Commun. Comput. Phys.
doi: 10.4208/cicp.171109.070510a

Vol. **9**, No. 2, pp. 324-362
February 2011

Approximate Riemann Solvers and Robust High-Order Finite Volume Schemes for Multi-Dimensional Ideal MHD Equations

Franz Georg Fuchs[1,*], Andrew D. McMurry[1], Siddhartha Mishra[2], Nils Henrik Risebro[1] and Knut Waagan[3]

[1] *Centre of Mathematics for Applications, University of Oslo, P.O. Box 1053, Blindern N-0316 Oslo, Norway.*
[2] *Seminar for Applied Mathematics, D-Math, ETH Zürich, HG G. 57.2, Rämistrasse 101, Zürich-8092, Switzerland.*
[3] *Center for Scientific Computation and Mathematical Modeling, The University of Maryland, CSCAMM 4146, CSIC Building #406, Paint Branch Drive College Park, MD 20742-3289, USA.*

Received 17 November 2009; Accepted (in revised version) 7 May 2010

Communicated by Chi-Wang Shu

Available online 27 August 2010

Abstract. We design stable and high-order accurate finite volume schemes for the ideal MHD equations in multi-dimensions. We obtain excellent numerical stability due to some new elements in the algorithm. The schemes are based on three- and five-wave approximate Riemann solvers of the HLL-type, with the novelty that we allow a varying normal magnetic field. This is achieved by considering the semi-conservative Godunov-Powell form of the MHD equations. We show that it is important to discretize the Godunov-Powell source term in the right way, and that the HLL-type solvers naturally provide a stable upwind discretization. Second-order versions of the ENO- and WENO-type reconstructions are proposed, together with precise modifications necessary to preserve positive pressure and density. Extending the discrete source term to second order while maintaining stability requires non-standard techniques, which we present. The first- and second-order schemes are tested on a suite of numerical experiments demonstrating impressive numerical resolution as well as stability, even on very fine meshes.

AMS subject classifications: 35L65, 74S10, 65M12

Key words: Conservation laws, MHD, divergence constraint, Godunov-Powell source terms, upwinded source terms, high-order schemes.

*Corresponding author. *Email addresses:* franzf@math.uio.no (F. G. Fuchs), a.d.mcmurry@ifi.uio.no (A. D. Mcmurry), smishra@sam.math.ethz.ch (S. Mishra), nilshr@math.uio.no (N. H. Risebro), knutwa@ucar.edu (K. Waagan)

1 Introduction

Many interesting problems in astrophysics, solar physics and engineering involve macroscopic plasma models and are usually described by the equations of ideal magnetohydrodynamics (MHD).

1.1 Derivation of the equations

In macroscopic plasma models, the variables of interest are the mass density of the plasma ρ, the velocity field $\mathbf{u}=(u_1,u_2,u_3)^T$, the magnetic field $\mathbf{B}=(B_1,B_2,B_3)^T$, the pressure p and the total energy E. The unknowns obey the following conservation (balance) laws (see [36] for details),

1. Conservation of mass: mass of a plasma is conserved, resulting in

$$\rho_t+\mathrm{div}(\rho\mathbf{u})=0.$$

2. Faraday's law: the magnetic flux across a surface $\mathbf{S}$ bounded by a curve $\delta\mathbf{S}$ is given by Faraday's law

$$-\frac{d}{dt}\int_S \mathbf{B}\cdot\mathbf{dS}=\int_{\delta S} E\cdot dl.$$

By using Stokes Theorem and the fact that the electric field in a co-moving frame is zero and assuming zero resistivity, Faraday's law leads to

$$\mathbf{B}_t+\mathrm{curl}(\mathbf{B}\times\mathbf{u})=-\mathbf{u}(\mathrm{div}\mathbf{B}). \tag{1.1}$$

The above equation is termed the magnetic induction equation and can also be written in the divergence form

$$\mathbf{B}_t+\mathrm{div}(\mathbf{u}\otimes\mathbf{B}-\mathbf{B}\otimes\mathbf{u})=-\mathbf{u}(\mathrm{div}\mathbf{B}).$$

3. Conservation of momentum: in differential form, the conservation of momentum is

$$(\rho\mathbf{u})_t+\mathrm{div}(\rho\mathbf{u}\otimes\mathbf{u}+p\mathcal{I})=\mathbf{J}\times\mathbf{B},$$

where $\mathbf{J}$ denotes the current density and $\mathcal{I}$ the 3×3 identity matrix. The Lorentz force exerted by the magnetic field is given by $\mathbf{J}\times\mathbf{B}$. Under the assumptions of ideal MHD, Ampere's law expresses the current density as

$$\mathbf{J}=\mathrm{curl}(\mathbf{B}).$$

Using standard vector identities results in the following semi-conservative form,

$$(\rho\mathbf{u})_t+\mathrm{div}\Big(\rho\mathbf{u}\otimes\mathbf{u}+\Big(p+\frac{1}{2}\mathbf{B}^2\Big)\mathcal{I}-\mathbf{B}\otimes\mathbf{B}\Big)=-\mathbf{B}(\mathrm{div}\mathbf{B}).$$

4. Conservation of energy: defining the hydrodynamic energy of an ideal gas as

$$E^{\rm hd}=\frac{p}{\gamma-1}+\frac{1}{2}\rho\mathbf{u}^2,$$

and using the conservation of this energy results in

$$E_t^{\rm hd}+{\rm div}\big((E^{\rm hd}+p)\mathbf{u}\big)=\mathbf{J}\cdot(\mathbf{B}\times\mathbf{u}).$$

The right hand side represents the change in energy due to the magnetic field. By using standard vector identities and Ampere's law, we obtain

$$\mathbf{J}\cdot(\mathbf{B}\times\mathbf{u})=\Big(\mathbf{B}\cdot\frac{\partial\mathbf{B}}{\partial t}-(\mathbf{u}\cdot\mathbf{B})({\rm div}\mathbf{B})-{\rm div}(\mathbf{B}\cdot\mathbf{B})\mathbf{u}-(\mathbf{u}\cdot\mathbf{B})\mathbf{B}\Big).$$

Defining the total energy of the plasma as

$$E=E^{\rm hd}+\frac{1}{2}\mathbf{B}^2,$$

energy conservation takes the form

$$E_t+{\rm div}\Big(\Big(E+p+\frac{1}{2}\mathbf{B}^2\Big)\mathbf{u}-(\mathbf{u}\cdot\mathbf{B})\mathbf{B}\Big)=-(\mathbf{u}\cdot\mathbf{B})({\rm div}\mathbf{B}).$$

Combining all the above balance laws leads to the *semi-conservative* form of the ideal MHD equations

$$\rho_t+{\rm div}(\rho\mathbf{u})=0, \tag{1.2a}$$

$$(\rho\mathbf{u})_t+{\rm div}\Big(\rho\mathbf{u}\otimes\mathbf{u}+\Big(p+\frac{1}{2}|\mathbf{B}|^2\Big)I-\mathbf{B}\otimes\mathbf{B}\Big)=-\mathbf{B}({\rm div}\mathbf{B}), \tag{1.2b}$$

$$\mathbf{B}_t+{\rm div}(\mathbf{u}\otimes\mathbf{B}-\mathbf{B}\otimes\mathbf{u})=-\mathbf{u}({\rm div}\mathbf{B}), \tag{1.2c}$$

$$E_t+{\rm div}\Big(\Big(E+p+\frac{1}{2}|\mathbf{B}|^2\Big)\mathbf{u}-(\mathbf{u}\cdot\mathbf{B})\mathbf{B}\Big)=-(\mathbf{u}\cdot\mathbf{B})({\rm div}\mathbf{B}). \tag{1.2d}$$

The semi-conservative form (1.2) is also called the *Godunov-Powell form*, and the source on the right-hand side of (1.2) is termed the *Godunov-Powell source term*.

Magnetic monopoles have not been observed in nature (although their existence has been hypothesized in a number of quantum regimes by both the unified field theory as well as string theory). Hence, it is common to assume that the magnetic field is solenoidal, i.e., it satisfies the divergence constraint

$${\rm div}(\mathbf{B})\equiv 0. \tag{1.3}$$

Under this constraint, the source terms in (1.2) are zero and the constraint is explicitly added to the equations to obtain the *conservative* form of the ideal MHD equations

$$\rho_t + \mathrm{div}(\rho\mathbf{u}) = 0, \tag{1.4a}$$

$$(\rho\mathbf{u})_t + \mathrm{div}\Big(\rho\mathbf{u}\otimes\mathbf{u} + \Big(p + \frac{1}{2}|\mathbf{B}|^2\Big) I - \mathbf{B}\otimes\mathbf{B}\Big) = 0, \tag{1.4b}$$

$$\mathbf{B}_t + \mathrm{div}(\mathbf{u}\otimes\mathbf{B} - \mathbf{B}\otimes\mathbf{u}) = 0, \tag{1.4c}$$

$$E_t + \mathrm{div}\Big(\Big(E + p + \frac{1}{2}|\mathbf{B}|^2\Big)\mathbf{u} - (\mathbf{u}\cdot\mathbf{B})\mathbf{B}\Big) = 0, \tag{1.4d}$$

$$\mathrm{div}(\mathbf{B}) = 0. \tag{1.4e}$$

Taking divergence on both sides of the magnetic induction equation (1.1) yields

$$(\mathrm{div}\mathbf{B})_t + \mathrm{div}\big(\mathbf{u}(\mathrm{div}\mathbf{B})\big) = 0. \tag{1.5}$$

This means that any solenoidal initial magnetic field remains divergence free. Hence, for smooth solutions, the semi-conservative form (1.2) is equivalent to the standard form (1.4), provided that the initial magnetic field is divergence free.

Despite their formal equivalence, the two forms, (1.4) and (1.2), differ in some respects. We believe that it is more natural to consider and discretize the semi-conservative form (1.2), since the derivation from first principles gives (1.2). Furthermore, (1.2) is *Galilean invariant*, whereas the standard form (1.4) is not.

From a mathematical perspective, the semi-conservative form (1.2) was shown to be *symmetrized* by the physical entropy in [20], leading to stability estimates [6]. The standard form (1.4) is not *symmetrizable* and it is not clear if it is possible to obtain any well-posedness results for (1.4), whereas estimates on the entropy may pave the way for obtaining well-posedness results for the symmetrizable form (1.2) (see [6]).

The standard form (1.4) (semi-conservative form (1.2)) is a system of conservation (balance) laws. Eigenvalue analysis, see [6, 37], shows that the system is hyperbolic but not strictly hyperbolic. Solutions are quite complicated and contain interesting discontinuities like shock waves, contact discontinuities, compound and intermediate shocks. Even for "simple" initial value problems, such as the Riemann problem, we do not have existence or well-posedness results. This means that numerical simulations are the main tools to study solutions of these equations.

1.2 Survey of available numerical methods

Finite volume schemes are among the most efficient and widely used numerical methods for the numerical solution of conservation (balance) laws. In these methods (see [28, 42]), the computational domain is divided into cells, and cell-averages of the conserved quantities are evolved by integrating the balance law over the cell. The update requires numerical fluxes, defined in terms of exact or approximate solutions of Riemann problems

(along the normal direction) at each cell interface. Higher-order spatial accuracy is recovered by employing non-oscillatory piecewise polynomial reconstructions like second-order TVD [26, 27, 50], higher-order ENO [23] and WENO [40] methods. Higher-order temporal accuracy results from using stability-preserving Runge-Kutta methods [22].

Finite volume schemes for the MHD equations have been employed with a fair amount of success. The Riemann problem is too complicated to solve exactly [47], and approximate Riemann solvers are employed to define numerical fluxes. Linearized solvers of the Roe-type [12, 37] have been devised but often give negative pressures and densities, see [18] for examples. An alternative is to use approximate Riemann-solvers of the HLL-type [24]. These solvers approximate the wave-structure of the Riemann problem (consisting up to eight waves), by a smaller number of waves. The standard HLL solver leads to excessive smearing at the contact discontinuities (see [18, 19] for numerical experiments) and motivates the design of approximate Riemann solvers modeling contact discontinuities. For hydrodynamics, these HLL type three wave solvers are denoted as HLLC solvers and were proposed in [43, 44]. Three-wave HLL solvers for MHD have been designed in [8, 21, 25, 30, 31]. Further refinements on this theme include the design of five-wave solvers that also approximate Alfvén waves in [8, 34]. Some of these HLL type solvers [8, 21, 34] are proved to preserve positive pressures and densities. They also typically ensure that the second law of thermodynamics is not violated, referred to as entropy stability, which is not easily achieved with linearized solvers. Numerical results showing the robustness of these HLL-solvers, particularly in one space dimension, have been presented, see [8,34]. We remark that Roe-type Riemann solvers are compatible with the algorithmic framework presented later in this paper, and would conceivably benefit from it.

However, the extension of one-dimensional numerical fluxes to multi-dimensional MHD in standard form (1.4) is not straightforward. The divergence constraint (1.3) in one-dimension implies that the normal magnetic field must be a *constant* in space. HLL-type solvers like the ones described in [21, 34] use this information in their definitions of speeds and states. For multi-dimensional MHD, the magnetic field in each normal direction is *no longer constant*. Consequently, it is not trivial to extend the HLL-solvers in this case. One possible solution consists in using an average of the normal magnetic field across each interface in the expressions. This somewhat arbitrary choice may destroy the stability properties of the solvers.

Another highly non-trivial and related aspect in several dimensions is the treatment of the divergence constraint $\mathrm{div}\mathbf{B} = 0$. Standard finite volume schemes will generate divergence errors, and these can induce instabilities, see [49]. A popular method to remove divergence is the projection method of [10], based on solving elliptic equations at every time step. These methods are computationally very expensive.

A popular divergence cleaning method consists in staggering the discretizations of the velocity and magnetic field, leading to methods with a (discrete) divergence free magnetic field. Variants of this method have been proposed in [2, 13, 16, 32, 33, 38, 39, 41, 45, 46, 49] and references therein. Staggering of the variables leads to complications when

parallelizing the method, and in designing variable grid methods. It must be noted that controlling a particular discrete form of the divergence does not generally lead to any control on other discrete forms as the solutions of the ideal MHD equations are not necessarily smooth. Therefore, in the presence of shocks, the values of a particular discrete form do not necessarily imply anything about the quality of the simulation results. Examples illustrating this phenomenon are presented in [17, 49].

Another potential problem with both the staggering and projection techniques lies in their numerical stability. The nonlinear stability analysis techniques (i.e., entropy stability, positivity) that have been quite successful for finite volume schemes do not apply directly to such methods. In a recent paper [18], we provided examples where the projection method was quite stable on coarse meshes, but exhibited instabilities when the mesh was refined. We have also observed similar behavior for some staggered mesh methods.

A third alternative for divergence cleaning was proposed in [35] and consists of discretizing the semi-conservative Godunov-Powell form (1.2). In [35,36], a linearized solver is used to define numerical fluxes and a simple centered discretization is proposed for the Godunov-Powell source term in (1.2). Note that (1.5) suggests the initial divergence (scaled with the density) errors will be transported out of the domain by the flow. In a recent paper [17], examples were constructed showing that a centered discretization of the Godunov-Powell source term can lead to numerical instabilities, even for the simple case of the linear magnetic induction equation (1.1). Hence, the Godunov-Powell source term has to be suitably "upwinded" to obtain stable discretizations. A related method is the Generalized Lagrange multiplier method of [14].

The above discussion brings out the relative strengths and weaknesses of the three available methods for divergence cleaning. All the three methods might lead to problems with numerical stability. It is mostly manifested on very fine meshes as the numerical diffusion is not sufficient to stabilize the schemes. Since the projection method can be computationally expensive and staggering based methods are quite complicated to implement on parallel computers (and with adaptive mesh refinement), we focus on a stable approximation of the semi-conservative Godunov-Powell form (1.2). The fact that this form is Galilean invariant and symmetrizable makes it particularly desirable to discretize. We are also motivated by related approaches in [8, 51] and [17], which contain stability estimates not available for staggered schemes, as well as strong numerical evidence of robustness. Note that a straightforward central discretization of the source term may be unstable, so we will *upwind* the source term in a suitable manner.

1.3 Aims and scope of this paper

Our aim in this paper is to design a robust and high-order accurate finite volume scheme for the semi-conservative form (1.2) of ideal MHD in multi-dimensions. Our numerical algorithm consists of the following ingredients:

• We derive three-wave and five-wave HLL type approximate Riemann solvers for the semi-conservative form (1.2). The fluxes are defined in terms of approximate solu-

tions to Riemann problems (in the normal direction) at each interface. The main difference between existing solvers and our approach lies in the fact that we allow the normal magnetic field to vary across the interface. The resulting solvers extend the three-wave HLL solver of [21] and the highly popular five-wave HLL solver of [34] to non-constant normal magnetic fields and hence trivially to multi-dimensions.

• We discretize the Godunov-Powell source term in (1.2) by using the states and speeds of the HLL solvers to calculate the source term in each direction. This is simply and naturally achieved by taking the usual cell averages. Thus, the source term is automatically upwinded.

• Second-order spatial accuracy is obtained by designing suitable ENO and WENO-type reconstructions. Standard ENO-WENO reconstructions have been used to obtain high-order accurate schemes for the MHD equations, see [4,5,48] and references therein. However, these reconstructions have to be modified to ensure that the resulting schemes preserve positive pressures and densities. We rely on the results of [7] and of a recent paper [51] to design these modifications.

• The upwind discrete Godunov-Powell source term is extended to second order with techniques from [1] and [51].

• Second-order temporal accuracy is obtained by using Runge-Kutta methods.

The above ingredients are combined to obtain a second-order finite volume scheme for MHD equations (1.2) in multi-dimensions. The resulting schemes are very simple to implement. Although we are unable to provide rigorous stability proofs, we verify the resulting schemes on a wide variety of benchmark numerical experiments. The numerical results on a sequence of meshes (including very fine meshes) demonstrate that both the first- and the second-order versions of our schemes are numerically stable.

As stated earlier, stability is the key to numerically resolve details on very fine meshes. We would like to mention that highly resolved solutions are not widely reported in the literature, leaving the stability at those resolutions open for questioning.

Related discretizations of a modified (partial) form of (1.2) based on operator splitting and on relaxation were proposed in [18] and [9] respectively. The solvers of [9] were proved to be positivity preserving and entropy stable. Second-order positivity preserving extensions of this approach have been presented and tested in a recent paper [51].

The rest of this paper is organized as follows: the numerical schemes are presented in Section 2 and the numerical experiments are reported in Section 3.

2 Numerical schemes

For notational simplicity, we focus on the semi-conservative form of the MHD equations (1.2) in two space dimensions

$$\mathbf{W}_t+\mathbf{f}(\mathbf{W})_x+\mathbf{g}(\mathbf{W})_y=\mathbf{s}^1(\mathbf{W},\mathbf{W}_x)+\mathbf{s}^2(\mathbf{W},\mathbf{W}_y), \tag{2.1}$$

where

$$\mathbf{W}=(\rho,\rho u_1,\rho u_2,\rho u_3,B_1,B_2,B_3,E)^T,$$

is the vector of conserved variables, and the fluxes are given by

$$\mathbf{f}(\mathbf{W})=\begin{pmatrix}\rho\\ \rho u_1^2+\pi_1-\frac{B_1^2}{2}\\ \rho u_1u_2-B_1B_2\\ \rho u_1u_3-B_1B_3\\ 0\\ u_1B_2-u_2B_1\\ u_1B_3-u_3B_1\\ (E+\pi_1)u_1-u_1\frac{B_1^2}{2}-B_1(u_2B_2+u_3B_3)\end{pmatrix},$$

$$\mathbf{g}(\mathbf{W})=\begin{pmatrix}\rho\\ \rho u_1u_2-B_1B_2\\ \rho u_2^2+\pi_2-\frac{B_2^2}{2}\\ \rho u_1u_3-B_1B_3\\ u_2B_1-u_1B_2\\ 0\\ u_2B_3-u_3B_2\\ (E+\pi_2)u_2-u_2\frac{B_2^2}{2}-B_2(u_1B_1+u_3B_3)\end{pmatrix},$$

where we have defined

$$\pi_1=p+\frac{B_2^2+B_3^2}{2}, \tag{2.2a}$$

$$\pi_2=p+\frac{B_1^2+B_3^2}{2}. \tag{2.2b}$$

Similarly, the Godunov-Powell source terms in (1.2) can be written explicitly as

$$\mathbf{s}^1(\mathbf{W},\mathbf{W}_x)=\begin{pmatrix}0,\\ -\left(\frac{B_1^2}{2}\right)_x\\ -B_2(B_1)_x\\ -B_3(B_1)_x\\ -u_1(B_1)_x\\ -u_2(B_1)_x\\ -u_3(B_1)_x\\ -u_1\left(\frac{B_1^2}{2}\right)_x-(u_2B_2+u_3B_3)(B_1)_x\end{pmatrix},$$

$$\mathbf{s}^2(\mathbf{W},\mathbf{W}_y)=\begin{pmatrix} 0, \\ -B_1(B_2)_y \\ -\left(\frac{B_2^2}{2}\right)_y \\ -B_3(B_2)_y \\ -u_1(B_2)_y \\ -u_2(B_2)_y \\ -u_3(B_2)_y \\ -u_2\left(\frac{B_2^2}{2}\right)_y-(u_1B_1+u_3B_3)(B_2)_y \end{pmatrix}.$$

Note that we have used the chain rule

$$B_1(B_1)_x=\left(\frac{B_1^2}{2}\right)_x \quad \text{and} \quad B_2(B_2)_y=\left(\frac{B_2^2}{2}\right)_y.$$

While true for smooth solutions, this formula may no longer hold when the magnetic field has discontinuities. However, using this formulation proved to be robust in practice.

We approximate (2.1) in a domain

$$\mathbf{x}=(x,y)\in[X_l,X_r]\times[Y_b,Y_t],$$

for simplicity, the domain is discretized by a uniform grid in both directions with mesh sizes Δx and Δy, respectively. We set

$$x_i=X_l+i\Delta x, \quad y_j=Y_b+j\Delta y \quad \text{and} \quad I_{i,j}=\left[x_{i-\frac{1}{2}},x_{i+\frac{1}{2}}\right)\times\left[y_{j-\frac{1}{2}},y_{j+\frac{1}{2}}\right).$$

The cell average of the unknown vector $\mathbf{W}$ at time t^n in the cell $I_{i,j}$ is denoted $\mathbf{W}_{i,j}^n$.

A standard finite volume scheme (first-order in both space and time) is obtained by integrating the balance law (2.1) over the cell $I_{i,j}$ and the time interval $[t^n,t^{n+1}]$, with $t^{n+1}=t^n+\Delta t^n$, where the time-step Δt^n is determined by a suitable CFL condition. The resulting fully-discrete form of the scheme is

$$\mathbf{W}_{i,j}^{n+1}=\mathbf{W}_{i,j}^n-\frac{\Delta t^n}{\Delta x}\left(\mathbf{F}_{i+\frac{1}{2},j}^n-\mathbf{F}_{i-\frac{1}{2},j}^n\right)-\frac{\Delta t^n}{\Delta y}\left(\mathbf{G}_{i,j+\frac{1}{2}}^n-\mathbf{G}_{i,j-\frac{1}{2}}^n\right)+\Delta t^n(\mathbf{S}_{i,j}^1+\mathbf{S}_{i,j}^2). \tag{2.3}$$

The flux

$$\mathbf{F}_{i+\frac{1}{2},j}^n=\mathbf{F}(\mathbf{W}_{i,j}^n,\mathbf{W}_{i+1,j}^n),$$

and the source $\mathbf{S}_{i,j}^1$ are hence determined from a solution to the following Riemann problem

$$\mathbf{W}_t+\mathbf{f}(\mathbf{W})_x=\mathbf{s}^1(\mathbf{W},\mathbf{W}_x), \qquad \mathbf{W}(x,0)=\begin{cases} \mathbf{W}_L, & x<0, \\ \mathbf{W}_R, & x>0. \end{cases} \tag{2.4}$$

Similarly, the flux $\mathbf{G}$ and the approximation of the Godunov-Powell source term $\mathbf{S}^2$ are given in terms of a Riemann problem in the y-direction. The Riemann problem (2.4)

has an intricate solution involving up to eight waves. Therefore the solution to (2.4) is in practice replaced by a so called approximate Riemann solver (see, e.g., [28]). The purpose of this section is to derive two such solvers. They will be given as functions of x/t (as the exact solution of (2.4) is self-similar), and we must ensure local conservation in order to end up with a scheme of the semi-conservative form (2.3).

2.1 Three-wave HLL solver

To derive this solver we follow the approach of [21, 43]. The approximate solution and fluxes for (2.4) are given by

$$\mathbf{W}^{\text{HLL3}} = \begin{cases} \mathbf{W}_L, & \text{if } x/t \le s_L, \\ \mathbf{W}_L^*, & \text{if } s_L < x/t < s_M, \\ \mathbf{W}_R^*, & \text{if } s_M < x/t < s_R, \\ \mathbf{W}_R, & \text{if } s_R \le x/t, \end{cases} \tag{2.5a}$$

$$\mathbf{F}^{\text{HLL3}}(\mathbf{W}_L,\mathbf{W}_R) = \begin{cases} \mathbf{F}_L, & \text{if } x/t \le s_L, \\ \mathbf{F}_L^*, & \text{if } s_L < x/t < s_M, \\ \mathbf{F}_R^*, & \text{if } s_M < x/t < s_R, \\ \mathbf{F}_R, & \text{if } s_R \le x/t. \end{cases} \tag{2.5b}$$

Note that we do not enforce $\mathbf{F}=\mathbf{f}(\mathbf{W})$ for any of the flux components involving π_1 as we allow π_1 of (2.2) to be a free variable. It plays a role similar to the relaxation pressure in [8]. For consistency, we set

$$\pi_1 = p + \frac{B_2^2 + B_3^2}{2}$$

in $\mathbf{F}_L$ and $\mathbf{F}_R$. The outer wave speeds s_L and s_R model the fast magneto-sonic waves and are defined as in [15, 21], i.e.,

$$s_L = \min\left\{u_{1L} - c_{fL}, \bar{u}_1 - \bar{c}_f\right\}, \qquad s_R = \max\left\{u_{1R} + c_{fR}, \bar{u}_1 + \bar{c}_f\right\}, \tag{2.6}$$

where $\bar{u}_1$ and $\bar{c}_f$ are the normal velocity and the fast wave speed of the Jacobian matrix $A((\mathbf{W}_L+\mathbf{W}_R)/2)$ respectively. This choice is important for numerical stability and accuracy.

In order to describe the solver, we need to determine the speed of the middle wave s_M and the intermediate states $\mathbf{W}_L^*, \mathbf{W}_R^*$. We follow [21] in letting the middle wave model a material contact discontinuity. Hence, the velocity field and the tangential magnetic fields are assumed to be constant across the middle wave. This allows defining

$$\mathbf{u}^* = \mathbf{u}_L^* = \mathbf{u}_R^*, \quad B_2^* = B_{2L}^* = B_{2R}^* \quad \text{and} \quad B_3^* = B_{3L}^* = B_{3R}^*.$$

Furthermore, the difference in our solver and the three-wave solver of [21] lies in the fact that we consider a non-constant normal magnetic field B_1. The normal magnetic field B_1

only jumps across the middle wave (modeling the linear degenerate "divergence wave" implied by (1.5)) and is constant across the outer waves.

We will impose local conservation across each wave to determine the various states. Local conservation across the outermost waves means that

$$s_L\mathbf{W}_L^*-\mathbf{F}_L^*=s_L\mathbf{W}_L-\mathbf{F}_L,\qquad s_R\mathbf{W}_R-\mathbf{F}_R=s_R\mathbf{W}_R^*-\mathbf{F}_R^*. \tag{2.7}$$

Conservation across the middle wave s_M involves taking the source term $\mathbf{s}^1$ in (2.4) into account. The conservation relation is given by

$$s_M\mathbf{W}_R^*-s_M\mathbf{W}_L^*=\mathbf{F}_R^*-\mathbf{F}_L^*+\mathbf{s}^{1,*}, \tag{2.8}$$

where

$$\mathbf{s}^{1,*}=\begin{pmatrix} 0 \\ -\frac{(B_{1R})^2-(B_{1L})^2}{2} \\ -B_2^*(B_{1R}-B_{1L}) \\ -B_3^*(B_{1R}-B_{1L}) \\ -\mathbf{u}^*(B_{1R}-B_{1L}) \\ -u_1^*\frac{(B_{1R})^2-(B_{1L})^2}{2}-(u_2^*B_2^*+u_3^*B_3^*)(B_{1R}-B_{1L}) \end{pmatrix}, \tag{2.9}$$

amounts to integrating the source $\mathbf{s}^1$ in (2.4) across the middle wave (as described in the next section). The above expression follows from the assumption that B_1 jumps only across the middle wave while the velocity field and tangential components of the magnetic field remain constant. The use of the source term in the above conservation relations is the key difference in our approach and the one used in [21].

For any middle speed s_M, a straightforward application of the conservation relations (2.7) and (2.8) determine unique values of intermediate densities given by

$$\rho_\theta^*=\rho_\theta\frac{u_{1\theta}-s_\theta}{s_M-s_\theta},\qquad \theta\in\{L,R\}. \tag{2.10}$$

Using conservation across all the three waves (adding (2.7) and (2.8)), results in the global conservation relation

$$\mathbf{F}_R-\mathbf{F}_L=s_R\mathbf{W}_R-s_L\mathbf{W}_L+(s_M-s_R)\mathbf{W}_R^*+(s_L-s_M)\mathbf{W}_L^*+\mathbf{s}^{1,*}. \tag{2.11}$$

We can use the intermediate density states (2.10) and global conservation (2.11) to obtain

$$s_M=u_1^*=\frac{\pi_{1R}-\pi_{1L}+\rho_Ru_{1R}(u_{1R}-s_R)-\rho_Lu_{1L}(u_{1L}-s_L)}{\rho_R(u_{1R}-s_R)-\rho_L(u_{1L}-s_L)}.$$

Similarly, one uses local conservation (2.7) across the two outer waves to obtain the intermediate "relaxed" pressures

$$\pi_{1\theta}^*=\pi_{1\theta}+\rho_\theta(u_{1\theta}-s_\theta)(u_{1\theta}-s_M), \tag{2.12}$$

for $\theta\in\{L,R\}$. Note that conservation across the middle wave automatically implies that $\pi^*_{1L}=\pi^*_{1R}$, and that (2.12) confirms this assertion. The next step is to determine the tangential velocity and magnetic field. Using global conservation across the wave fan (2.11), we obtain that the intermediate values u^*_σ and B^*_σ satisfy the following two linear equations

$$\alpha u^*_\sigma-\beta B^*_\sigma=c_\sigma,\qquad -\beta u^*_\sigma-\zeta B^*_\sigma=d_\sigma,\qquad \sigma\in\{2,3\},$$

where

$$c_\sigma=\rho_R u_{\sigma R}(u_{1R}-s_R)-\rho_L u_{\sigma L}(u_{1L}-s_L)-(B_{1R}B_{\sigma R}-B_{1L}B_{\sigma L}), \tag{2.13a}$$
$$d_\sigma=B_{\sigma R}(s_R-u_{1R})-B_{\sigma L}(s_L-u_{1L})-(B_{1L}u_{\sigma L}-B_{1R}u_{\sigma R}), \tag{2.13b}$$
$$\alpha=\rho_R(u_{1R}-s_R)-\rho_L(u_{1L}-s_L),\qquad \zeta=s_R-s_L,\qquad \beta=B_{1R}-B_{1L}. \tag{2.13c}$$

Solving the linear system (2.13), the intermediate tangential components of velocity and magnetic field are obtained as

$$u^*_\sigma=\frac{\zeta c_\sigma-\beta d_\sigma}{\alpha\zeta+\beta^2},\qquad B^*_\sigma=\frac{-\alpha d_\sigma-\beta c_\sigma}{\alpha\zeta+\beta^2}. \tag{2.14}$$

Remark 2.1. In general, the denominator; $\alpha\zeta+\beta^2$, in (2.14) can become small, leading to a degeneracy in the states. A simple calculation shows that

$$\alpha\zeta+\beta^2\neq 0$$

if

$$\left(\rho_R c^R_f+\rho_L c^L_f\right)(s_R-s_L)>(B_{1R}-B_{1L})^2.$$

This condition can be ensured by "widening" the wave fan slightly by modifying the fast wave speeds in (2.6). The resulting conditions are

$$s_R\geq u_{1R}+\frac{1}{2}\left(\max\left\{(u_{1L}-u_{1R}),0\right\}\right)+\widetilde{c}_{fR}, \tag{2.15a}$$
$$s_L\leq u_{1L}-\frac{1}{2}\left(\max\left\{(u_{1L}-u_{1R}),0\right\}\right)-\widetilde{c}_{fL}, \tag{2.15b}$$

where

$$\widetilde{c}^2_{f\theta}=\frac{\gamma p_\theta}{\rho_\theta}+\frac{B^2_{1\theta}}{\rho_\theta}(1+\epsilon)+\frac{B^2_{2\theta}+B^2_{3\theta}}{\rho_\theta}+\sqrt{\left(\frac{\gamma p_\theta+|\mathbf{B}|^2_\theta}{\rho_\theta}\right)^2-4\frac{\gamma p_\theta B^2_{1\theta}}{\rho^2_\theta}},\quad \theta\in\{L,R\},$$

for some small positive ϵ. Using the conditions (2.15) to widen the wave fan ensures that the denominator $\alpha\zeta+\beta^2$ is never zero and the states are well defined.

Finally, the intermediate total energy states are determined by local conservation relations (2.7) to be

$$E^*_\theta=\frac{E_\theta(u_{1\theta}-s_\theta)+\pi_{1\theta}u_{1\theta}-\pi^*_{1\theta}s_M+\frac{B^2_{1\theta}}{2}(u_{1\theta}-s_M)+B_{1\theta}(B_{2\theta}u_{2\theta}+B_{3\theta}u_{3\theta}-B^*_{2\theta}u^*_{2\theta}-B^*_{3\theta}u^*_{3\theta})}{s_M-s_\theta},$$

for $\theta \in \{L,R\}$. Hence, all the intermediate states are determined explicitly. The intermediate fluxes are obtained in terms of the intermediate states by local conservation (2.7)

$$\mathbf{F}_L^* = \mathbf{F}_L + s_L(\mathbf{W}_L^* - \mathbf{W}_L), \qquad \mathbf{F}_R^* = \mathbf{F}_R + s_R(\mathbf{W}_R^* - \mathbf{W}_R). \tag{2.16}$$

Combining the above expressions for the states and the fluxes, we write down our explicit flux formula for the three-wave solver as

$$\mathbf{F}^{H_3}_{i+\frac{1}{2},j} = \begin{cases} \mathbf{F}_{i,j}, & \text{if } \ s_{L,i+\frac{1}{2},j} > 0, \\ \mathbf{F}^*_{i,j}, & \text{if } \ s_{L,i+\frac{1}{2},j} \le 0 \ \text{ and } \ s_{M,i+\frac{1}{2},j} \ge 0, \\ \mathbf{F}^*_{i+1,j}, & \text{if } \ s_{M,i+\frac{1}{2},j} < 0 \ \text{ and } \ s_{R,i+\frac{1}{2},j} \ge 0, \\ \mathbf{F}_{i+1,j}, & \text{if } \ s_{R,i+\frac{1}{2},j} < 0. \end{cases} \tag{2.17}$$

Note that this may be discontinuous at $s_{M,i+1/2,j} = 0$ according to (2.8). Hence our choice of $\mathbf{F}^{H_3}$ in that case is merely a convention. It is the proper addition of the source term which ensures that the scheme is continuous.

In order to compute the fluxes in (2.17), we compute the intermediate states and speeds by (2.10), (2.12) and (2.14) and use the conservation relations (2.16) to obtain the numerical flux.

Remark 2.2. If we assume that the normal magnetic field B_1 is constant, i.e.,

$$B_{1L} = B_{1R},$$

then the three-wave solver defined above reduces to the three-wave solver derived in [21]. Hence, our three-wave solver extends the standard three-wave solver of [21] for the case of a non-constant normal magnetic field.

2.2 Discretization of the Godunov-Powell source term

In this section, we explain why we must have the jump condition (2.8) across the middle wave, and specify the discrete source $\mathbf{S}^{1,n}_{i,j}$ in (2.3). The discrete source must be consistent with the Godunov-Powell source term in x-direction $\mathbf{s}^1(\mathbf{W},\mathbf{W}_x)$. It will be determined from our solution of the Riemann problem (2.4) along the x-direction at the cell interfaces $(x_{i+1/2},y_j)$. The three-wave HLL approximate Riemann solver of the previous section provide us with the assumptions we need. The normal magnetic field jumps only across the contact-discontinuity modeled by the middle wave, while the velocity field and the tangential components of the magnetic field are constant across the middle wave.

Across the middle wave, $\mathbf{u}$, B_2 and B_3 are constant, in which case we may rewrite the balance law in (2.4) as a conservation law. The conservation law has the form

$$\mathbf{W}_t + \mathbf{F}(\mathbf{W})_x + \big(T(\mathbf{u},\mathbf{B})B_1\big)_x = 0$$

with

$$T(\mathbf{u},\mathbf{B})=\Big(0,\frac{B_1}{2},B_2,B_3,\mathbf{u},\frac{u_1B_1}{2}+u_2B_2+u_3B_3\Big)^{\top}.$$

By local evaluation, T takes the values T_L^* and T_R^* on each respective side of the middle wave. Local conservation is given by the Rankine-Hugoniot relations, which dictate that

$$s_M\mathbf{W}_R^*-s_M\mathbf{W}_L^*=\mathbf{F}_R^*-\mathbf{F}_L^*+T_R^*-T_L^*. \tag{2.18}$$

The relation (2.8) then follows from noting that

$$T_R^*-T_L^*=\mathbf{s}^{1,*},$$

again using the constancy of $\mathbf{u}$, B_2 and B_3.

The numerical update in cell i, $\mathbf{W}_i^{n+1}$ (we drop the y-dependence for this particular argument. Integration in the y-direction will be taken care of by the midpoint rule) is given in the standard manner (e.g., [28]) by letting the piecewise constant data $\mathbf{W}_i^n$ evolve according to the approximate Riemann solver $\mathbf{W}^{HLL3}$ for a time interval Δt^n (short enough to avoid wave interactions), then taking new cell averages of the conserved quantities. Using the conservation relations (2.7)-(2.8), we get that this amounts to

$$\mathbf{W}_i^{n+1}=\mathbf{W}_i^n-\frac{\Delta t^n}{\Delta x}\big(\mathbf{F}^n_{i+\frac{1}{2}}-\mathbf{F}^n_{i-\frac{1}{2}}\big)+\Delta t^n\mathbf{S}_i^{1,n}, \tag{2.19}$$

where

$$\mathbf{S}_i^{1,n}=\mathbf{s}^{1,*}_{i-\frac{1}{2}}\mathbf{1}_{\left\{\left(s_{M,i-\frac{1}{2}}\geq 0\right)\right\}}+\mathbf{s}^{1,*}_{i+\frac{1}{2}}\mathbf{1}_{\left\{\left(s_{M,i+\frac{1}{2}}<0\right)\right\}}, \tag{2.20}$$

and the numerical fluxes are given by (2.17). For the case that $s_{M,i+1/2,j}=0$ our choice here was dictated by our choice in (2.17). This completes the description of the numerical fluxes and sources in the x-direction.

We emphasize that the discrete Godunov-Powell source term in each cell consists of contributions from Riemann solutions at the bordering interfaces and depends on the sign of the middle wave at each interface. Thus, the Godunov-Powell source term is suitably upwinded. Note that assuming the normal magnetic field B_1 to be constant for the whole domain leads to the source term being zero. This approach is novel and is very different from the usual centered discretization of the Godunov-Powell source term (see [36] and other references therein). A related *upwind* discretization of a partial form of the source term s^1 was presented in [9]. There are analogies between the above upwind discretization of the Godunov-Powell source term and upwinding the non-conservative source term in Shallow water equations with bottom topography [1].

Remark 2.3. As stated earlier, when the normal magnetic field is constant, i.e., $B_{1L}=B_{1R}$, the three-wave solver presented here reduces to the HLLC three-wave solver of [21],

which is shown to preserve positive pressure and density. When the normal magnetic field is no longer constant, we are unable to provide a rigorous proof that the three-wave solver preserves positive pressure and density. However, extensive numerical testing illustrates that upwinding the source term leads to a scheme that preserves positive density and pressure.

2.3 Five-wave HLL solver

The three-wave solver of the previous section does not model Alfvén waves precisely, and instead diffuse these waves more than necessary. Alfvén waves can be approximated better by extending the three-wave solver to an HLL type five-wave solver. In addition to the three waves with wave speeds s_L, s_R and s_M, we add two new waves with speeds s_L^* and s_R^* respectively with the requirement that

$$s_L \leq s_L^* \leq s_M \leq s_R^* \leq s_R.$$

Hence, solution of the Riemann problem at each interface is approximated by four intermediate states $\mathbf{W}_L^*$, $\mathbf{W}_L^{**}$, $\mathbf{W}_R^{**}$ and $\mathbf{W}_R^*$. A five-wave solver for ideal MHD equations with constant normal magnetic fields was developed in [34] and we will extend this solver to the case of non-constant normal magnetic fields below.

The outer-wave speeds s_L and s_R are determined by (2.6) (using the correction (2.15)) as in the three-wave solver. We assume that the normal velocity is constant across the three inner waves, i.e.,

$$s_M = u_{1L}^* = u_{1L}^{**} = u_{1R}^{**} = u_{1R}^*, \tag{2.21}$$

as the inner waves model a contact discontinuity and Alfvén waves, and the normal velocity remains constant across all three of them. Similarly, the waves with speeds s_L^* and s_R^* model Alfvén waves. Hence, as in [34], the density and the "relaxed" pressures are constant across them leading to

$$\rho_\theta^{**} = \rho_\theta^*, \qquad \pi_{1\theta}^{**} = \pi_{1\theta}^*, \qquad \theta \in \{L,R\}.$$

Furthermore, the wave with speed s_M models a contact discontinuity and the tangential components of the velocity and the magnetic field remain constant across it leading to

$$u_{\sigma L}^{**} = u_{\sigma R}^{**} = u_\sigma^{**}, \qquad B_{\sigma L}^{**} = B_{\sigma R}^{**} = B_\sigma^{**}, \tag{2.22}$$

for $\sigma \in \{2,3\}$. The normal magnetic field should only jump across the middle wave, i.e.,

$$B_{1\theta}^* = B_{1\theta}^{**} = B_{1\theta}, \qquad \theta \in \{L,R\}. \tag{2.23}$$

As a result of (2.22) and (2.23), the Godunov-Powell source term takes the same form as in (2.9) with u_σ^*, B_σ^* being replaced by u_σ^{**} and B_σ^{**}, for $\sigma \in \{2,3\}$. We denote this source term by $\mathbf{s}^{1,**}$.

Using local conservation (2.7) across the outermost waves and (2.21), we obtain unique values of ρ^*_θ of the form,

$$\rho^*_\theta = \rho_\theta \frac{u_{1\theta}-s_\theta}{s_M-s_\theta}, \qquad \theta \in \{L,R\}. \tag{2.24}$$

Conservation across the entire wave fan leads to the following relation

$$\begin{aligned}\mathbf{F}_R-\mathbf{F}_L =& s_R\mathbf{W}_R - s_L\mathbf{W}_L + (s^*_R-s_R)\mathbf{W}^*_R + (s_M-s^*_R)\mathbf{W}^{**} \\ &+ (s^*_L-s_M)\mathbf{W}^{**}_L + (s_L-s^*_L)\mathbf{W}^*_L + \mathbf{s}^{1,**}.\end{aligned} \tag{2.25}$$

We can use the intermediate density states (2.24) and global conservation (2.25) to obtain the following expression for the middle speed

$$u^*_{1,L} = u^*_{1,R} = s_M = \frac{\pi_{1R}-\pi_{1L}+\rho_R u_{1R}(u_{1R}-s_R)-\rho_L u_{1L}(u_{1L}-s_L)}{\rho_R(u_{1R}-s_R)-\rho_L(u_{1L}-s_L)}.$$

Note that this is the same expression as the middle speed in the three-wave solver. Similarly, one uses local conservation (2.7) across the two outer waves to obtain the intermediate "relaxed" pressures

$$\pi^*_{1\theta} = \pi_{1\theta} + \rho_\theta(u_{1\theta}-s_\theta)(u_{1\theta}-s_M),$$

for $\theta \in \{L,R\}$. Note that $\pi^*_{1L} = \pi^*_{1R}$. Following [34], we can use conservation across the outer-most waves (2.7) and obtain a system of two linear equations for $u^*_{\sigma\theta}$ and $B^*_{\sigma\theta}$, for $\sigma = \{2,3\}$. These equations can be explicitly solved to obtain

$$u^*_{\sigma\theta} = u_{\sigma\theta} + \frac{B_{1\theta}B_{\sigma\theta}(u_{1\theta}-s_M)}{\rho_\theta(u_{1\theta}-s_\theta)(s_M-s_\theta)-(B_{1\theta})^2}, \tag{2.26a}$$

$$B^*_{\sigma\theta} = B_{\sigma\theta}\frac{\rho_\theta(u_{1\theta}-s_\theta)^2-(B_{1\theta})^2}{\rho_\theta(u_{1\theta}-s_\theta)(s_M-s_\theta)-(B_{1\theta})^2}. \tag{2.26b}$$

Remark 2.4. The denominator in the above states (2.26) can become zero. This will typically occur in the degenerate case that the Alfvén speed $|B_1|/\sqrt{\rho}$ approaches the fast speed c_f. Therefore, it is natural to switch to the three-wave solver of the previous section, when

$$\left|\rho_\theta(u_{1\theta}-s_\theta)(s_M-s_L)-(B_{1\theta})^2\right| < \epsilon\rho_\theta c^2_{f\theta}$$

for some small $\epsilon > 0$.

The intermediate energy states can be determined by local conservation (2.7) as

$$E^*_\theta = \frac{E_\theta(u_{1\theta}-s_\theta)+\pi_{1\theta}u_{1\theta}-\pi^*_{1\theta}s_M+\frac{B^2_{1\theta}}{2}(u_{1\theta}-s_M)+B_{1\theta}(B_{2\theta}u_{2\theta}+B_{3\theta}u_{3\theta}-B^*_{2\theta}u^*_{2\theta}-B^*_{3\theta}u^*_{3\theta})}{s_M-s_\theta},$$

for $\theta\in\{L,R\}$. The local conservation relations across the new waves imply that

$$s_L^*=s_M-\frac{|B_{1L}|}{\sqrt{\rho_L^*}},\qquad s_R^*=s_M+\frac{|B_{1R}|}{\sqrt{\rho_R^*}}.$$

Hence the Alfvén wave speeds are accurately represented. Note that we use essentially the same Alfvén speeds as in [34], but account for the variation of the normal magnetic field across the contact discontinuity. Furthermore, conservation across the new waves reduces to

$$B_\sigma^{**}-B_{\sigma L}^*=\text{sign}(B_{1L})\sqrt{\rho_L^*}(u_\sigma^{**}-u_{\sigma L}^*), \tag{2.27a}$$

$$B_\sigma^{**}-B_{\sigma R}^*=-\text{sign}(B_{1L})\sqrt{\rho_R^*}(u_\sigma^{**}-u_{\sigma R}^*). \tag{2.27b}$$

These relations are identical to the exact Alfvén wave jump conditions. They imply that

$$u_\sigma^{**}=\frac{\text{sign}(B_{1L})\sqrt{\rho_L^*}u_{\sigma L}^*+\text{sign}(B_{1R})\sqrt{\rho_R^*}u_{\sigma R}^*+B_{\sigma R}^*-B_{\sigma L}^*}{\text{sign}(B_{1L})\sqrt{\rho_L^*}+\text{sign}(B_{1R})\sqrt{\rho_R^*}}, \tag{2.28a}$$

$$B_\sigma^{**}=\frac{\text{sign}(B_{1L})\sqrt{\rho_R^*}B_{\sigma L}^*+\text{sign}(B_{1R})\sqrt{\rho_L^*}B_{\sigma R}^*+\sqrt{\rho_L^*\rho_R^*}(u_{\sigma R}^*-u_{\sigma L}^*)}{\text{sign}(B_{1L})\sqrt{\rho_R^*}+\text{sign}(B_{1R})\sqrt{\rho_L^*}}. \tag{2.28b}$$

Remark 2.5. Observe that if

$$\text{sign}(B_{1R})\neq\text{sign}(B_{1L})\quad\text{and}\quad\rho_R^*=\rho_L^*, \tag{2.29}$$

the relations (2.27) can not be solved, and the formulas (2.28) break down. In this case, we relax to the HLL three-wave solver of the previous section. This should be seen in light of the discontinuity in the jump conditions (2.27) in the non strictly hyperbolic case $B_1=0$. Furthermore, if $B_{1L}=0$ and $B_{1R}\neq0$ or vice versa, we get meaningful formulas, but we need to check that the jump conditions across the middle wave hold. They become

$$S_M\mathbf{W}_L^*-\mathbf{F}_L^*=S_M\mathbf{W}_R^{**}-\mathbf{F}_R^{**}+\mathbf{s}^{1,**},$$

which is easily verified. When $B_{1L}=B_{1R}=0$, it simply means that $s_L^*=s_M=s_R^*$, hence we do not need to calculate the $**$-states. The jump conditions are again easily verified, if we assume that the source $\mathbf{s}^{1,**}$ is zero (which is the limiting value away from (2.29)). Hence, the numerical fluxes and sources can be calculated in the same manner as for non-zero B_1.

Finally, the remaining energy states are given by conservation across the Alfvén waves resulting in

$$E_\theta^{**}=E_\theta^*+\frac{B_{1\theta}(B_{2\theta}^*u_{2\theta}^*+B_{3\theta}^*u_{3\theta}^*-B_2^{**}u_2^{**}-B_3^{**}u_3^{**})}{s_\theta^*-s_M},$$

for $\theta \in \{L,R\}$. This completes a description of the states of the five-wave solver. The corresponding fluxes can be determined by local conservation and the numerical flux is obtained similar to the formula (2.17). We remark that whenever $B_{1L} = B_{1R}$, the above solver reduces to the five-wave solver derived in [34].

For the discretization of the corresponding Godunov-Powell source term in this case, we use exactly the same arguments as in the case of the three-wave solver (as B_1 jumps only across the middle wave where the velocity and the tangential magnetic fields are constant) to obtain that

$$\mathbf{S}^{1,n}_{i,j} = \mathbf{s}^{1,**}_{i-\frac{1}{2},j}\mathbf{1}\left\{\left(s_{M,i-\frac{1}{2},j}\geq 0\right)\right\} + \mathbf{s}^{1,**}_{i+\frac{1}{2},j}\mathbf{1}\left\{\left(s_{M,i+\frac{1}{2},j}< 0\right)\right\},$$

where $\mathbf{s}^{1,**}_{i\pm 1/2,j}$ is defined as in (2.9) with the $**$ replacing the $*$ states.

2.4 Fluxes and sources in the y-direction

We have completed a description of the numerical flux $\mathbf{F}$ and discretized source $\mathbf{S}^1$ in the x-direction. In order to complete the scheme (2.3), we need to specify the numerical flux in the y-direction $\mathbf{G}$ and the corresponding Godunov-Powell source term $\mathbf{S}^2$. This is straightforward as the form of equations in each direction is similar.

The numerical flux $\mathbf{G}$ is defined in terms of both a three-wave solver and a five-wave solver. The three-wave solver is analogous to the states and fluxes obtained in (2.5) with normal velocity u_2 and normal magnetic field B_2. Similarly, the discretized source term $\mathbf{S}^2$ is similar to $\mathbf{S}^1$ defined in (2.20). The only change is to replace the normal velocity and magnetic fields to u_2 and B_2 respectively. The five-wave solver is analogously defined. The specification of $\mathbf{G},\mathbf{S}^2$ completes the description of the scheme (2.3).

2.5 Second-order accurate schemes

The finite volume scheme (2.3) is first-order accurate in both space and time. For practical applications, we need higher order of accuracy. We will design a finite volume scheme based on (2.3) that is second-order accurate in both space and time. The semi-discrete form of this scheme is given by

$$\frac{d}{dt}\mathbf{W}_{i,j} = \boldsymbol{\mathcal{F}}_{i,j} = -\frac{1}{\Delta x}\left(\mathbf{F}_{i+\frac{1}{2},j} - \mathbf{F}_{i-\frac{1}{2},j}\right) - \frac{1}{\Delta y}\left(\mathbf{G}_{i,j+\frac{1}{2}} - \mathbf{G}_{i,j-\frac{1}{2}}\right) + \widetilde{\mathbf{S}}^1_{i,j} + \widetilde{\mathbf{S}}^2_{i,j}, \tag{2.30}$$

where $\mathbf{W}_{i,j}(t)$ is the cell-average of the unknown at time t. We will define the numerical fluxes $\mathbf{F},\mathbf{G}$ and the sources $\widetilde{\mathbf{S}}^1,\widetilde{\mathbf{S}}^2$ below.

It is standard [28] to replace the piecewise constant approximation $\mathbf{W}_{i,j}$ with non-oscillatory piecewise linear reconstructions in-order to obtain second-order spatial accuracy. There are a variety of reconstructions including the popular TVD-MUSCL limiters [50]. We will use second-order ENO reconstruction [23] and WENO reconstruction [40] as these procedures can be easily extended to obtain even higher-order schemes.

2.5.1 ENO Reconstruction

Given the cell averages $\mathbf{W}_{i,j}$, we reconstruct in the primitive variables

$$\mathbf{V}_{i,j}=\left\{\rho_{i,j},\mathbf{u}_{i,j},\mathbf{B}_{i,j},p_{i,j}\right\}.$$

Define the ENO-differences in each direction as

$$D^x\mathbf{V}_{i,j}=\begin{cases}\mathbf{V}_{i+1,j}-\mathbf{V}_{i,j}, & \text{if } \Gamma^x_{i,j}\leq 1,\\ \mathbf{V}_{i,j}-\mathbf{V}_{i-1,j}, & \text{otherwise,}\end{cases}\qquad D^y\mathbf{V}_{i,j}=\begin{cases}\mathbf{V}_{i,j+1}-\mathbf{V}_{i,j}, & \text{if } \Gamma^y_{i,j}\leq 1,\\ \mathbf{V}_{i,j}-\mathbf{V}_{i,j-1}, & \text{otherwise,}\end{cases}$$

where

$$\Gamma^x_{i,j}=\frac{\left|\psi(\mathbf{V}_{i+1,j})-\psi(\mathbf{V}_{i,j})\right|}{\left|\psi(\mathbf{V}_{i,j})-\psi(\mathbf{V}_{i-1,j})\right|},\qquad \Gamma^y_{i,j}=\frac{\left|\psi(\mathbf{V}_{i,j+1})-\psi(\mathbf{V}_{i,j})\right|}{\left|\psi(\mathbf{V}_{i,j})-\psi(\mathbf{V}_{i,j-1})\right|},$$

and ψ for some function ψ called the global smoothness indicator. A good global smoothness indicator is a function of the conserved variables that serves to indicate all possible discontinuities in the solution. The density serves as a good global smoothness indicator for hydrodynamics. However, it is difficult to identify a single indicator for all possible discontinuities in MHD. We use global smoothness indicator, $\psi(\mathbf{V})=E$ as the total energy jumps across all types of discontinuities for the Riemann problem corresponding to one-dimensional MHD.

The reconstructed piecewise linear function is each cell $I_{i,j}$ is denoted by

$$\overline{\mathbf{V}}_{i,j}(x,y)=\mathbf{V}_{i,j}+\frac{1}{\Delta x}D^x\mathbf{V}_{i,j}(x-x_i)+\frac{1}{\Delta y}D^y\mathbf{V}_{i,j}(y-y_j).$$

The reconstructed conservative variables can be easily obtained by transforming the reconstructed primitive variables.

2.5.2 WENO procedure

As an alternative to the above reconstruction, consider the following cell-gradients

$$\begin{aligned}\bar{D}^x\mathbf{V}_{i,j}&=\Big(\omega^x_{i,j}\left(\mathbf{V}_{i+1,j}-\mathbf{V}_{i,j}\right)+\left(1-\omega^x_{i,j}\right)\left(\mathbf{V}_{i,j}-\mathbf{V}_{i-1,j}\right)\Big),\\ \bar{D}^y\mathbf{V}_{i,j}&=\Big(\omega^y_{i,j}\left(\mathbf{V}_{i,j+1}-\mathbf{V}_{i,j}\right)+\left(1-\omega^y_{i,j}\right)\left(\mathbf{V}_{i,j}-\mathbf{V}_{i,j-1}\right)\Big),\end{aligned}$$

where the weights are given by

$$\begin{aligned}\omega^x_{i,j}&=\frac{a^0_{i,j}}{a^0_{i,j}+a^1_{i,j}},\qquad a^0_{i,j}=\frac{1}{3(\epsilon+\beta^{x,0}_{i,j})},\qquad a^1_{i,j}=\frac{2}{3(\epsilon+\beta^{x,1}_{i,j})},\\ \omega^y_{i,j}&=\frac{b^0_{i,j}}{b^0_{i,j}+b^1_{i,j}},\qquad b^0_{i,j}=\frac{1}{3(\epsilon+\beta^{y,0}_{i,j})},\qquad b^1_{i,j}=\frac{2}{3(\epsilon+\beta^{y,1}_{i,j})},\end{aligned}$$

where ϵ is a small positive number, and the parameters are given by

$$\beta^{x,0}_{i,j}=\big(\psi(\mathbf{V}_{i+1,j})-\psi(\mathbf{V}_{i,j})\big)^2,\qquad \beta^{x,1}=\big(\psi(\mathbf{V}_{i,j})-\psi(\mathbf{V}_{i-1,j})\big)^2,$$
$$\beta^{y,0}_{i,j}=\big(\psi(\mathbf{V}_{i,j+1})-\psi(\mathbf{V}_{i,j})\big)^2,\qquad \beta^{y,1}=\big(\psi(\mathbf{V}_{i,j})-\psi(\mathbf{V}_{i,j-1})\big)^2,$$

and the indicator function ψ is defined above. The corresponding linear reconstruction is given by

$$\underline{\mathbf{V}}_{i,j}(x,y)=\mathbf{V}_{i,j}+\frac{1}{\Delta x}\overline{D}^x\mathbf{V}_{i,j}(x-x_i)+\frac{1}{\Delta y}\overline{D}^y\mathbf{V}_{i,j}(y-y_j). \tag{2.31}$$

Note that the choice of weights implies that the WENO reconstruction (2.31) is third-order accurate for smooth solutions (at least in one-space dimension).

ENO and WENO reconstructions have been used extensively to compute approximate solutions of the ideal MHD equations (1.4) (see [5,48]) and other references therein. However, both the ENO and WENO reconstructions suffer from a common problem: the reconstructed densities and pressures may not be positive. Since the positivity of density and pressure is absolutely essential for obtaining any physically meaningful results, the reconstructions have to be modified further. A simple modification consists of further limiting the slope in either direction. Let $D^x\rho$ and D^xp be the ENO-gradients of density and pressure in the x-direction, we follow [23] and introduce the following clipping

$$D^{x,c}\rho_{i,j}=\max\Big\{-\overline{\omega}\rho_{i,j},\min\Big\{\overline{\omega},D^x\rho_{i,j}\Big\}\Big\}, \tag{2.32a}$$
$$D^{x,c}p_{i,j}=\max\Big\{-\overline{\omega}p_{i,j},\min\Big\{\overline{\omega},D^xp_{i,j}\Big\}\Big\}, \tag{2.32b}$$

where $\overline{\omega}<2$ is a positive parameter. Simple calculations show that the above modification ensures that the reconstructed pressure and density remain positive. We choose $\overline{\omega}=1.9$ in our simulations. Similarly in the y-direction, we have

$$D^{y,c}\rho_{i,j}=\max\Big\{-\overline{\omega}\rho_{i,j},\min\Big\{\overline{\omega},D^y\rho_{i,j}\Big\}\Big\},$$
$$D^{y,c}p_{i,j}=\max\Big\{-\overline{\omega}p_{i,j},\min\Big\{\overline{\omega},D^yp_{i,j}\Big\}\Big\}.$$

However, this only guarantees positivity of the reconstructed variables, not for the updated ones.

A further modification of the gradients was suggested in a recent paper [51] to ensure positivity preserving updated states. Denote

$$\big(D^{x,c}\mathbf{V}_{i,j},D^{y,c}\mathbf{V}_{i,j}\big)=\Big(\big\{D^{x,c}\rho_{i,j},D^x\mathbf{u}_{i,j},D^x\mathbf{B}_{i,j},D^{x,c}p_{i,j}\big\},\big\{D^{y,c}\rho_{i,j},D^y\mathbf{u}_{i,j},D^y\mathbf{B}_{i,j},D^{y,c}p_{i,j}\big\}\Big),$$

and

$$L^x_{i,j}=\frac{1}{8}\Big[\rho_{i,j}\Big(\big|D^x\mathbf{u}_{i,j}\big|^2+\big|D^x\mathbf{B}_{i,j}\big|^2+\frac{1}{2}\Big(\min\Big\{0,\rho_{i,j}\big(\mathbf{u}_{i,j}\cdot D^x\mathbf{u}_{i,j}\big)\Big\}\Big)\Big)\Big]+\frac{1}{2\rho_{i,j}}\big(D^{x,c}\rho_{i,j}\big)^2\big|D^x\mathbf{u}_{i,j}\big|^2,$$
$$L^y_{i,j}=\frac{1}{8}\Big[\rho_{i,j}\Big(\big|D^y\mathbf{u}_{i,j}\big|^2+\big|D^y\mathbf{B}_{i,j}\big|^2+\frac{1}{2}\Big(\min\Big\{0,\rho_{i,j}\big(\mathbf{u}_{i,j}\cdot D^y\mathbf{u}_{i,j}\big)\Big\}\Big)\Big)\Big]+\frac{1}{2\rho_{i,j}}\big(D^{y,c}\rho_{i,j}\big)^2\big|D^y\mathbf{u}_{i,j}\big|^2,$$
$$R_{i,j}=\frac{p_{i,j}}{\gamma-1}.$$

Then, we further modify the gradients by

$$\widehat{D}^x\mathbf{V}_{i,j}=D^{x,c}\mathbf{V}_{i,j}\sqrt{\frac{R_{i,j}}{\max\{L^x_{i,j},R_{i,j}\}}},\qquad \widehat{D}^y\mathbf{V}_{i,j}=D^{y,c}\mathbf{V}_{i,j}\sqrt{\frac{R_{i,j}}{\max\{L^y_{i,j},R_{i,j}\}}}. \tag{2.33}$$

Thus $\widehat{D}^x,\widehat{D}^y$ are the gradients that we use for the final reconstruction. In [51], it was shown that this results in a positive scheme provided that the underlying first-order scheme is positive, and a particular discretization of the source term is used. Various numerical experiments presented in [51] showed that there is no loss of accuracy when this positivity preserving modification is employed. We investigate this issue further in the section on numerical experiments and arrive at a similar conclusion.

The reconstructed states are now given by

$$\widehat{\mathbf{V}}_{i,j}(x,y)=\mathbf{V}_{i,j}+\frac{1}{\Delta x}\widehat{D}^x\mathbf{V}_{i,j}(x-x_i)+\frac{1}{\Delta y}\widehat{D}^y\mathbf{V}_{i,j}(y-y_j). \tag{2.34}$$

A similar procedure can be used for the WENO-gradients to obtain a modified WENO reconstruction.

The reconstructed primitive variables correspond to the reconstructed conservative function $\widehat{\mathbf{W}}_{i,j}(x,y)$. Define the point-values

$$\mathbf{W}^E_{i,j}=\widehat{\mathbf{W}}_{i,j}\big(x_{i+\frac{1}{2}},y_j\big),\qquad \mathbf{W}^W_{i,j}=\widehat{\mathbf{W}}_{i,j}\big(x_{i-\frac{1}{2}},y_j\big),$$
$$\mathbf{W}^N_{i,j}=\widehat{\mathbf{W}}_{i,j}\big(x_i,y_{j+\frac{1}{2}}\big),\qquad \mathbf{W}^S_{i,j}=\widehat{\mathbf{W}}_{i,j}\big(x_i,y_{j+\frac{1}{2}}\big).$$

We can use the above defined values to define the second-order numerical fluxes as

$$\mathbf{F}_{i+\frac{1}{2},j}=\mathbf{F}\big(\mathbf{W}^E_{i,j},\mathbf{W}^W_{i+1,j}\big),\qquad \mathbf{G}_{i,j+\frac{1}{2}}=\mathbf{G}\big(\mathbf{W}^N_{i,j},\mathbf{W}^S_{i,j+1}\big),$$

where $\mathbf{F}$ and $\mathbf{G}$ are given by either the three-wave solver or the five-wave solver of the previous section. Similarly, the second-order source terms can be calculated as

$$\mathbf{S}^1_{i,j}=\mathbf{s}^{1,*}_{i-\frac{1}{2},j}\mathbf{1}_{\left\{\left(s_{M,i-\frac{1}{2},j}\geq 0\right)\right\}}+\mathbf{s}^{1,*}_{i+\frac{1}{2},j}\mathbf{1}_{\left\{\left(s_{M,i+\frac{1}{2},j}<0\right)\right\}},$$

where $\mathbf{s}^{1,*}_{i+1/2,j}$ is defined as in (2.9), but with the values $\mathbf{W}_{i,j}$, $\mathbf{W}_{i+1,j}$ replaced by $\mathbf{W}^E_{i,j}$, $\mathbf{W}^W_{i+1,j}$. The source $\mathbf{S}^2_{i,j}$ in the y-direction is defined analogously. Observe that for smooth solutions, the discretized source $\mathbf{S}^1_{i,j}$ vanishes to truncation order with $(B^E_1)_{i,j}-(B^W_1)_{i+1,j}$. Hence, we need to add an extra term for second-order consistency. However, this term should vanish when $\mathbf{S}^1_{i,j}$ becomes significant at jumps (see e.g., [1] for an analogous situation). We suggest the following simple modification

$$\widetilde{\mathbf{S}}^1_{i,j}=\mathbf{S}^1_{i,j}+\begin{pmatrix}0\\ \mathbf{B}_{i,j}\\ \mathbf{u}_{i,j}\cdot\mathbf{B}_{i,j}\\ \mathbf{u}_{i,j}\end{pmatrix}\frac{1}{\Delta x}\widehat{D}^xB^1_{i,j}.$$

The term $\widetilde{\mathbf{S}}^2_{i,j}$ in the y-direction is analogously defined. This way of discretizing the source was found to be very stable in [51], while a similar but more complicated form also gave a provably positive scheme. Note that $\widetilde{\mathbf{S}}^{1,2}_{i,j}$, are consistent second-order discretizations of the Godunov-Powell source terms $\mathbf{s}^{1,2}$. Hence, we have completed a description of the (formally) second-order accurate in space semi-discrete scheme (2.30).

2.6 Time stepping

The standard scheme for a first order approximation in time is the forward-Euler time stepping, formally written

$$\mathbf{W}^{n+1}_{i,j} = \mathbf{W}^n_{i,j} + \Delta t^n \boldsymbol{\mathcal{F}}^n_{i,j},$$

where $\boldsymbol{\mathcal{F}}^n_i$ is defined in (2.30). For overall second-order schemes, we use the second-order strong-stability preserving Runge-Kutta (SSP) time stepping [22]

$$\begin{aligned}
\mathbf{W}^*_{i,j} &= \mathbf{W}^n_{i,j} + \Delta t^n \boldsymbol{\mathcal{F}}^n_{i,j},\\
\mathbf{W}^{**}_{i,j} &= \mathbf{W}^*_{i,j} + \Delta t^n \boldsymbol{\mathcal{F}}^*_{i,j},\\
\mathbf{W}^{n+1}_{i,j} &= \frac{1}{2}(\mathbf{W}^n_{i,j} + \mathbf{W}^{**}_{i,j}).
\end{aligned}$$

The time step is determined by a standard CFL condition. This completes our description of the finite volume schemes for (2.1).

3 Numerical experiments

We will validate the first- and second-order finite volume schemes on a series of numerical experiments in both one- and two-space dimensions. We test a total of six schemes:

H_3	First order with the three-wave HLL solver,
H_5	first order with the five-wave HLL solver,
H_3E	second order with three-wave HLL solver and ENO reconstruction,
H_3W	second order with three-wave HLL solver and WENO reconstruction,
H_5E	second order with five-wave HLL solver and ENO reconstruction,
H_5W	second order with five-wave HLL solver and WENO reconstruction.

All the second order schemes use the positivity preserving modifications (2.34). The first order schemes are evolved with a CFL number of 0.45 (which is theoretically sound due to excluding wave interactions in the cells), and the second order schemes use a CFL number of 0.9. In all our computations, we use $\gamma = 5/3$.

Regarding the measurement of errors, if we have a reference solution available, then we define the relative error as

$$100\times\frac{\left\|\alpha-\alpha_{\text{ref}}\right\|}{\left\|\alpha_{\text{ref}}\right\|},$$

where α is (a component of) the numerical approximation and α_{ref} is (the same component of) the reference solution, and $\|\cdot\|$ is some (usually L^1) norm.

3.1 Brio-Wu shock tube

This is a standard one-dimensional numerical test case for ideal MHD [11]. The initial conditions are given by

$$(\rho,\mathbf{u},\mathbf{B},p)=\begin{cases}(1,0,0,0,0.75,+1,0,1), & \text{if } x<0.5,\\ (0.125,0,0,0,0.75,-1,0,0.1), & \text{otherwise.}\end{cases}$$

The computational domain is $(x,t)\in[0,1]\times[0,0.5]$ with Neumann boundary conditions. Note that the normal magnetic field is constant. Therefore, the H_3 scheme and H_5 scheme reduce to the three wave and five wave solvers presented in [21] and [34] respectively. However, the four higher-order schemes are different from those presented in the literature. We present the density, computed with the H_3, H_5, H_3E and H_5W schemes at time $t=0.5$ in Fig. 1.

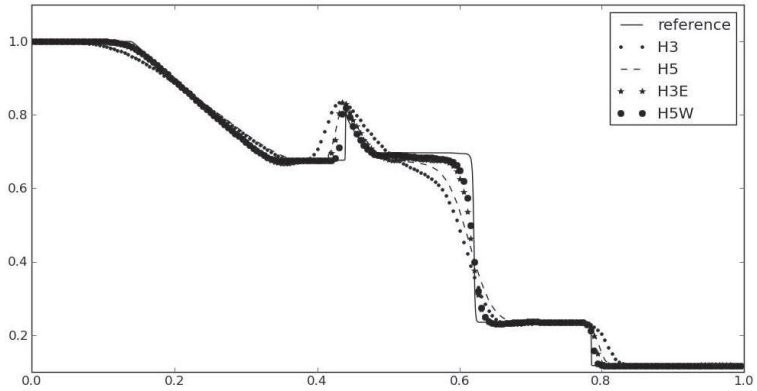

Figure 1: The computed density for the Brio-Wu shock tube with 200 grid points at $t=0.5$. Reference solution is the H_5W scheme with 3200 grid points.

The reference solution in this case is calculated with the H_5W second-order scheme on a mesh with 3200 points. The exact solution is quite complicated containing a shock wave, a contact discontinuity, a rarefaction wave and a *compound shock*. As expected, the H_5 scheme is more accurate than the H_3 schemes. Both the second-order schemes are clearly more accurate than the first-order schemes. The differences are also illustrated in Table 1, showing the relative percentage errors in the L^1 norm of the total energy on a

Table 1: Relative percentage errors for the total energy in L^1 at time $t=0.5$ and the order of convergence for the Brio-Wu shock tube for various mesh sizes M using the H_5W scheme with 3200 grid points as a reference solution.

M	H_3	rate	H_3E	rate	H_3W	rate	H_5	rate	H_5E	rate	H_5W	rate
50	2.2e-00		1.3e-00		1.3e-00		1.7e-00		1.2e-00		1.2e-00	
100	1.5e-00	0.6	7.9e-01	0.7	7.2e-01	0.9	1.2e-00	0.5	7.1e-01	0.8	6.5e-01	0.9
200	9.8e-01	0.6	5.0e-01	0.7	4.6e-01	0.6	7.4e-01	0.7	4.4e-01	0.7	4.1e-01	0.7
400	5.3e-01	0.9	1.9e-01	1.4	1.7e-01	1.4	3.7e-01	1.0	1.6e-01	1.5	1.4e-01	1.6
800	3.4e-01	0.6	1.1e-01	0.8	9.7e-02	0.8	2.2e-01	0.8	9.6e-02	0.7	8.3e-02	0.8
1600	1.9e-01	0.8	5.4e-02	1.0	4.4e-02	1.1	1.2e-01	0.9	4.8e-02	1.0	3.9e-02	1.1

sequence of meshes. The table confirms the observations obtained from the figure. Both the formal first-order accurate schemes have an average convergence rate close to 0.7. The second-order schemes are more accurate than the first-order schemes with considerably smaller errors. The H_5E and H_5W are slightly more accurate than the corresponding H_3E and H_3W scheme. The second-order schemes have an average rate of convergence around 1. This is to be expected as the solution contains discontinuities, and the order of accuracy deteriorates near these. This numerical experiment illustrates that the first and second-order schemes are able to capture complicated discontinuities like the compound shock quite well.

3.2 Super-fast expansion

A crucial stability criteria is the ability of a numerical scheme to preserve positive density and pressure. This numerical experiment [8, 18] is configured to highlight positivity aspects of schemes. We consider the one-dimensional form of the MHD equations (1.4) in the computational domain $[0,1]$ with initial data

$$(\rho,\rho\mathbf{u},p,\mathbf{B})=\begin{cases}(1.0,-3.1,0,0,0,0.5,0,,1.0), & \text{if } x<0.5,\\ (1.0,3.1,0,0,0,0.5,0,1.0), & \text{otherwise.}\end{cases}$$

The exact solution involves a super-fast expansion with one left moving rarefaction and one right moving rarefaction wave separated by a region of very low density and pressure. Linearized solvers like the Roe solver crash almost instantly on account of negative pressure [18].

Since the normal magnetic field is constant, the first-order H_3 and H_5 schemes reduce to the standard HLLC solver of [21] and HLLD solver of [34], respectively. These solvers are shown to be positivity preserving. The second-order H_3E, H_3W, H_5E and H_5W solvers are designed to preserve positive density and pressure. As we are unable to provide a rigorous proof of this fact, we test all the four second order schemes for the super-fast expansion and find them to be positivity preserving for all tested resolutions. Since there are no differences in results between the three- and five-wave solvers in this test case, we present the density, computed with H_3, H_3E and H_3W at time $t=0.1$ for 200

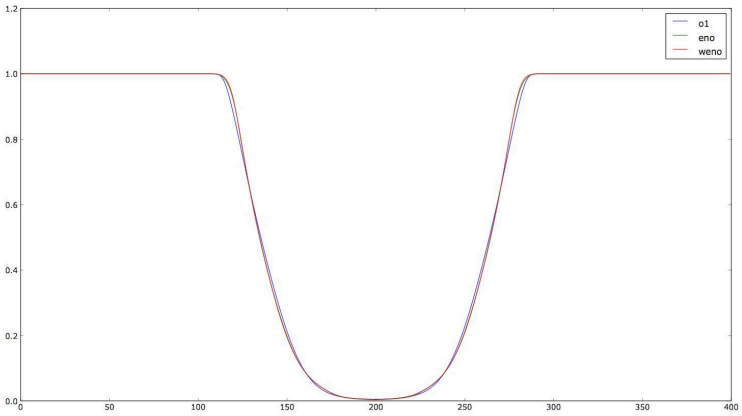

Figure 2: The pressure for super-fast expansion test with H_3,H_3E and H_3W solvers for 200 mesh points.

mesh points in Fig. 2. The results show that both the first and second order solvers preserve positivity. The second-order solvers are slightly more accurate than the first-order H_3 solver. Similar results were obtained for finer resolutions.

We remark that the positive preserving modifications (2.33) are absolutely essential to obtain stability. If we just use the clipping (2.32), the second-order schemes crash for very small times on account of negative pressures. This test further reinforces the case for modifying gradients in second-order reconstruction, as presented in [51].

3.3 Rotor problem

We start considering two-dimensional numerical experiments with this standard example (introduced in [2], considered in [49] among others). The computational domain is $(\mathbf{x},t)\in[0,1]^2\times[0,0.295]$, with Neumann boundary conditions. The initial data are given by

$$\rho=\begin{cases}10.0, & \text{if } r<0.1,\\ 1+9f(r), & \text{if } 0.1\leq r<0.115,\\ 1.0, & \text{otherwise,}\end{cases}$$

with

$$r(\mathbf{x})=\left|\mathbf{x}-(0.5,0.5)\right| \quad \text{and} \quad f(r)=\frac{23-200r}{3}.$$

The other variables are initially

$$(\rho u^1,\rho u^2)=\begin{cases}(-(10y-5)\rho,(10x-5)\rho), & \text{if } r<0.1,\\ (-(10y-5)f(r)\rho,(10x-5)f(r)\rho), & \text{if } 0.1\leq r<0.115,\\ (0.0,0.0), & \text{otherwise,}\end{cases}$$

$$(\rho u^3,B^1,B^2,B^3,p)=(0.0,2.5/\sqrt{\pi},0.0,0.0,0.5).$$

This describes a dense rotating region surrounded by static plasma with a uniform magnetic field. The pressure drops to very low values in the center. The main difficulty in the numerical solution of this problem is the low pressure, particularly on fine meshes. As stated in the introduction, most results presented in the literature show the approximation obtained on relatively coarse meshes. On coarse meshes, the numerical dissipation is large and provides some stability. However, computations on fine meshes lead to crashes due to negative pressures (see [18, 19] for illustrations of this). We compute with all the six schemes and show the computed pressures at time $t = 0.295$ and on a mesh with 200×200 mesh points in Fig. 3. The figure shows that both the first-order schemes provide a stable but diffusive approximation and the H_5 scheme is more accurate than the H_3 scheme. The second-order schemes are much more accurate and capture the shocks and smooth regions sharply at this resolution. For a more elaborate quantitative study of this problem, we compute solutions on a very fine 4000×4000 mesh and find that all the six schemes are stable and approximate the solution very well. We show the computed pressure with the H_5W scheme on a 4000×4000 mesh in Fig. 4 and use it as the reference solution.

We tabulate the relative percentage errors in L^1 for the pressure with respect to this reference solution and present them in Table 2. The table shows that the first-order H_5 scheme is (about thirty percent) more accurate than the first-order H_3 scheme. However, the second-order schemes are much more accurate than the first-order schemes. Sometimes, the gain in accuracy is an order of magnitude by using a second-order scheme. There is a gain in accuracy using the H_5 solver together with a second-order scheme. Similarly, the WENO-based schemes H_3W and H_5W are more accurate than their ENO-based counterparts. The observed rate of convergence for the first-order schemes is around 0.5 and that of the second-order schemes is better than 1 (except at the lowest resolutions). The results on coarse meshes are comparable to those displayed in [49] and other places in the literature. It was not possible to compare the results obtained on very fine meshes with existing schemes as very few papers present results on fine meshes (i.e., on meshes finer than 400 mesh points).

Table 2: Relative percentage errors in L^1 for the pressure at time $t = 0.295$ for the rotor problem for various mesh sizes M using the H_5W scheme on a 1600×1600 mesh as a reference solution.

M	H_3	rate	H_3E	rate	H_3W	rate	H_5	rate	H_5E	rate	H_5W	rate
50	10.0e-00		5.3e-00		5.1e-00		9.2e-00		4.6e-00		4.4e-00	
100	7.7e-00	0.4	3.1e-00	0.8	2.9e-00	0.8	6.6e-00	0.5	2.5e-00	0.9	2.3e-00	0.9
200	5.3e-00	0.5	1.6e-00	1.0	1.4e-00	1.1	4.5e-00	0.6	1.3e-00	0.9	1.1e-00	1.1
400	3.5e-00	0.6	7.6e-01	1.1	6.3e-01	1.2	2.8e-00	0.7	6.0e-01	1.1	5.1e-01	1.1
800	2.2e-00	0.7	3.5e-01	1.1	2.8e-01	1.2	1.7e-00	0.7	2.7e-01	1.2	2.0e-01	1.4

Another key issue in numerical simulations of multi-dimensional MHD is the behavior of div$B$. Note that the initial magnetic field is divergence free, hence the solutions of (2.1) are expected to remain divergence free. However, the schemes we use do not preserve any discrete divergence. We consider the standard second order discrete diver-

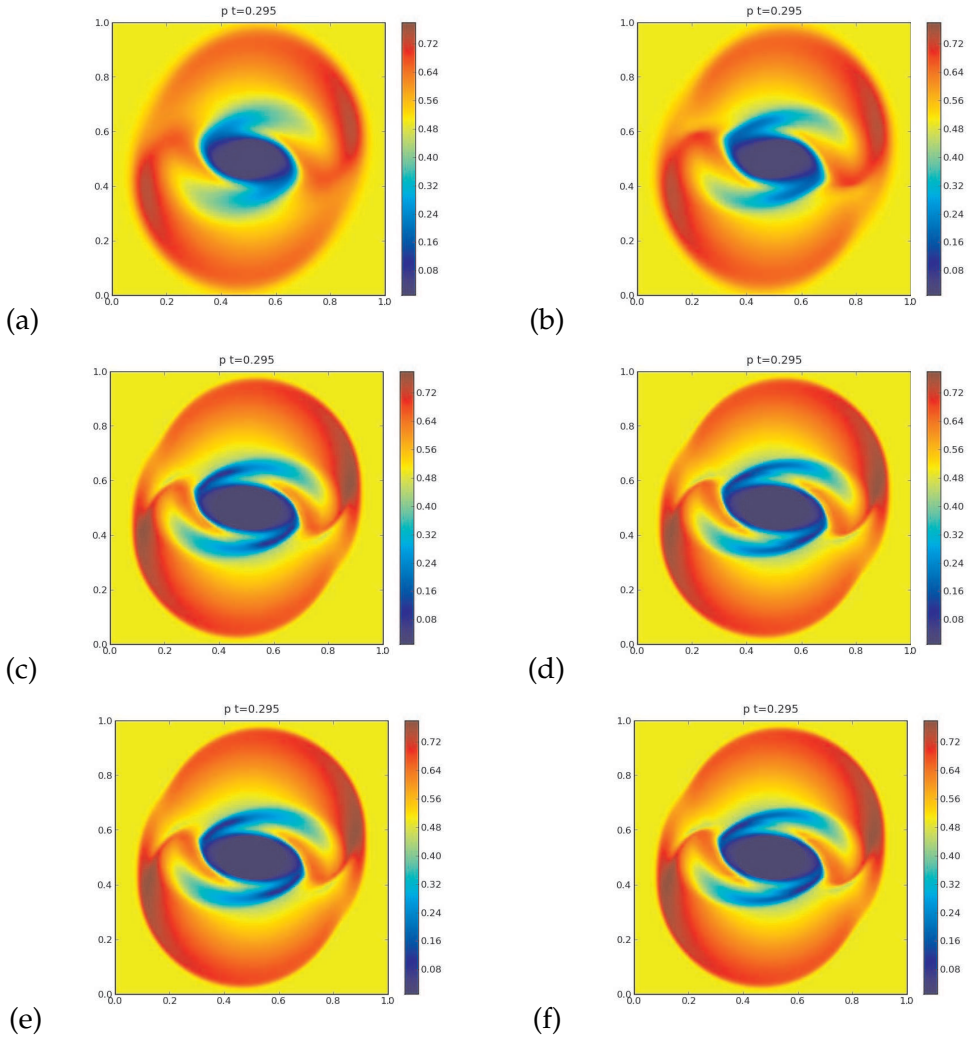

Figure 3: Pressure for the rotor problem on a 200×200 mesh at time $t=0.295$ all scaled to the extrema of the pressure obtained for a 200×200 mesh. (a) H_3; (b) H_5; (c) H_3E; (d) H_5E; (e) H_3W; (f) H_5W.

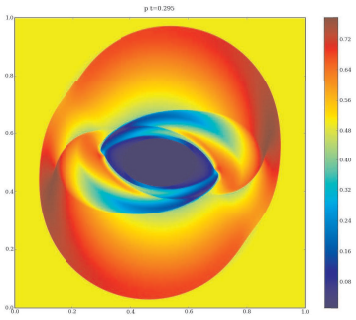

Figure 4: This figure shows the pressure for the rotor problem on a 4000×4000 mesh at time $t=0.295$ using the H_5W scheme.

Table 3: The L^1-norm of the discrete divergence at time $t=0.295$ for the rotor problem for various mesh sizes M.

M	H_3	H_3E	H_3W	H_5	H_5E	H_5W
50	2.2e-01	2.5e-01	2.1e-01	2.2e-01	2.4e-01	2.2e-01
100	1.7e-01	1.9e-01	1.8e-01	1.7e-01	2.0e-01	1.9e-01
200	1.4e-01	1.8e-01	1.6e-01	1.5e-01	1.9e-01	1.6e-01
400	1.3e-01	1.8e-01	1.5e-01	1.2e-01	1.6e-01	1.4e-01
800	1.1e-01	1.7e-01	1.5e-01	9.6e-02	1.5e-01	1.2e-01
1600	1.0e-01	1.6e-01	1.4e-01	8.2e-02	1.4e-01	1.2e-01

gence

$$\mathrm{div}(B)_{i,j}=\frac{(B_1)_{i+1,j}-(B_1)_{i-1,j}}{2\Delta x}+\frac{(B_2)_{i,j+1}-(B_2)_{i,j-1}}{2\Delta y} \tag{3.1}$$

and present the L^1 norm of the above discrete divergence in Table 3. As expected, all the six schemes produce a nonzero discrete divergence. However, the values are quite small, and seem to be decreasing with increasing mesh size, albeit quite slowly. Note that the divergence values are higher with the second-order schemes than with the first-order schemes. This is not unexpected as the second-order schemes resolve the shocks within fewer mesh points and hence generate a larger discrete divergence. These data primarily point towards the difficulty of numerically evaluating derivatives at under-resolved flow features. The key point is that divergence errors are not effecting the stability of the schemes as all the schemes are stable even at the finest mesh resolution of 4000×4000 mesh. This is unusual, and we have not come across other papers presenting solutions on comparable mesh sizes. As an example, the reference solutions in [49] were computed on a 400×400 mesh. We would like to point out that the positivity preserving modifications (2.32) and (2.33) are absolutely essential for stability of the second-order schemes. The computations crash almost immediately if these modifications are not employed. Similarly the upwinding of the source term in (1.2) is absolutely essential as the central discretization of this term leads to negative pressures almost immediately, even for the first-order schemes for fine mesh resolutions (see [18] for examples).

3.4 Orszag-Tang vortex

This commonly used benchmark test [49] has initial conditions given by

$$(\rho,\rho\mathbf{u},\mathbf{B},p)=\big(\gamma^2,-\gamma^2\sin(\pi y),\gamma^2\sin(\pi x),0,-\sin(\pi y),\sin(2\pi x),0,\gamma\big). \tag{3.2}$$

The computational domain is $(\mathbf{x},t)\in[0,2]^2\times[0,1]$ with periodic boundary conditions.

Even though the initial data are smooth, the solution develops shocks near the diagonals and a current sheet in the center of the domain. The solution also has interesting smooth features. We compute with all the six schemes and present the computed pressure at the final time on a 200×200 mesh in Fig. 5. Both the first-order H_3 and H_5 schemes are

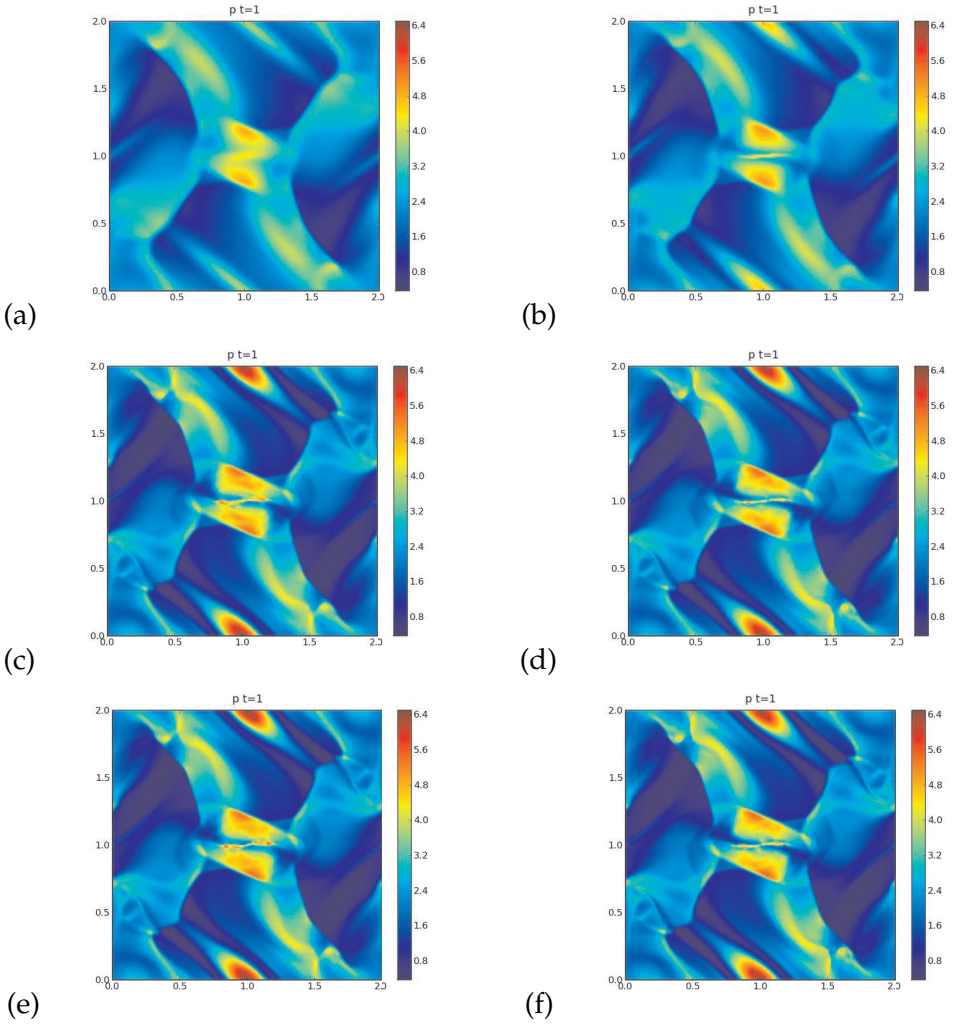

Figure 5: Pressure for the Orszag-Tang vortex on a 200×200 mesh at time $t=1$ scaled to the extrema of the pressure in the reference solution. (a) H_3; (b) H_5; (c) H_3E; (d) H_5E; (e) H_3W; (f) H_5W.

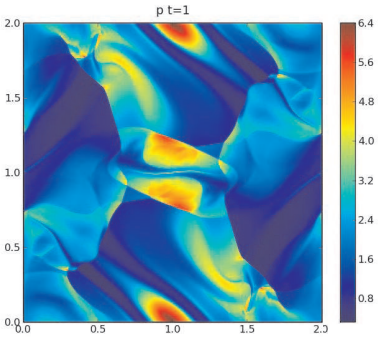

Figure 6: This figure shows the computed pressure for the Orszag-Tang vortex using the H_5W scheme on a 4000×4000 mesh at time $t=\pi$.

stable but dissipative. The shocks are smeared and the central vortex is not resolved. The H_5 scheme is better at approximating the solution than the H_3 scheme. The second-order schemes resolve the solution far better. The resolution of the shocks with the second-order schemes is very impressive. The smooth regions are also resolved quite accurately. We compute the a reference solution using the H_5W scheme on a 4000×4000 mesh. Fig. 6 shows the pressure of the reference solution. We observe that the H_5W scheme at this very fine mesh is stable and resolves the shocks as well as the central current sheet very well. Table 4 shows relative percentage L^1 errors in pressure on a sequence of meshes. As shown in the table, the first-order H_5 scheme has lower errors than the first-order H_3 scheme. Similarly, the second-order schemes significantly outperform (by an order of magnitude) the first-order schemes. In particular, the WENO-based schemes have lower errors than the ENO-based ones. Note that the second-order H_5W scheme is the most accurate with respect to the errors and has the best rate of convergence of about 1.3. The results are consistent with those obtained for the rotor problem.

Table 4: Percentage relative errors in L^1 for pressure at time $t=\pi$ for the Orszag-Tang vortex for various mesh sizes M using the H_5W scheme on a 1600×1600 mesh as a reference solution.

M	H_3	rate	H_3E	rate	H_3WE	rate	H_5	rate	H_5E	rate	H_5W	rate
50	3.6e+01		1.5e+01		1.4e+01		2.9e+01		1.2e+01		1.1e+01	
100	2.9e+01	0.3	8.8e-00	0.8	8.0e-00	0.8	2.3e+01	0.3	7.1e-00	0.8	6.2e-00	0.8
200	2.2e+01	0.4	5.0e-00	0.8	4.4e-00	0.9	1.6e+01	0.5	4.0e-00	0.8	3.4e-00	0.9
400	1.5e+01	0.6	2.6e-00	0.9	2.4e-00	0.9	1.1e+01	0.5	2.0e-00	1.0	1.6e-00	1.1
800	1.0e+01	0.6	1.5e-00	0.8	1.3e-00	0.9	7.2e-00	0.6	8.3e-01	1.3	5.9e-01	1.4

As in the rotor problem, we tabulate the L^1 discrete divergence (exact divergence is zero as we have divergence free initial data) in Table 5. The divergence values are low again and decrease very slowly (or remain constant) as the mesh is refined. Again, the discrete divergence values don't seem to affect the scheme's performance.

Table 5: Divergence in L^1 at time $t=\pi$ for the Orszag-Tang vortex for various mesh sizes M.

M	H_3	H_3E	H_3W	H_5	H_5E	H_5W
50	7.7e-02	2.5e-01	2.2e-01	1.5e-01	1.9e-01	1.7e-01
100	9.2e-02	2.6e-01	2.4e-01	1.6e-01	1.6e-01	1.5e-01
200	9.9e-02	2.7e-01	2.4e-01	1.4e-01	1.7e-01	1.5e-01
400	9.3e-02	2.0e-01	2.0e-01	1.3e-01	1.6e-01	1.3e-01
800	8.7e-02	1.8e-01	1.5e-01	1.1e-01	1.2e-01	1.0e-01
1600	8.4e-02	1.5e-01	1.2e-01	1.0e-01	1.0e-01	9.2e-02

3.5 Cloud-shock interaction

This is a benchmark test describing the interaction of a dense region (cloud) at rest with a moving shock. The computational domain is $(\mathbf{x},t)\in[0,1]^2\times[0,0.06]$ with artificial Neu-

mann type boundary conditions. The initial conditions consist of a shock moving to the right initially located at $x=0.05$, and a circular cloud of density $\rho=10$ and radius $r=0.15$ centered at $\mathbf{x}=(0.25,0.5)$

$$\rho=\begin{cases} 3.86859, & \text{if } x<0.05,\\ 10.0, & \text{if } \left|\mathbf{x}-(0.25,0.5)\right|<0.15,\\ 1.0, & \text{otherwise,}\end{cases}$$

$$\mathbf{u}=\begin{cases} (11.2536,0,0), & \text{if } x<0.05,\\ (1.0,0,0), & \text{otherwise,}\end{cases}$$

$$p=\begin{cases} 167.345, & \text{if } x<0.05,\\ 1.0, & \text{otherwise,}\end{cases}$$

$$\mathbf{B}=\begin{cases} (0,2.18261820,-2.18261820), & \text{if } x<0.05,\\ (0,0.56418958,0.56418958), & \text{otherwise.}\end{cases}$$

The cloud is initially in hydrostatic equilibrium with the surrounding fluid. The bubble stays stationary whereas the shock travels towards it, hits it and starts interacting with it. This interaction generates a bow shock in the front, tail shocks in the rear and we expect the creation of interesting turbulent-like structures where the cloud interacts with the shock. Again, we compute the solutions with all the six schemes and present numerical results of the total energy on a very fine mesh 1600×1600 mesh with all the six schemes in Fig. 7. The figure illustrates the stability of all the six schemes at this fine mesh resolution. The first-order schemes are a bit dissipative and do not approximate the turbulent like structures that are visible in the second order computations. The second order schemes are much more accurate with good resolution of the shocks as well as the turbulent-like structures in the bubble. The differences between the first-order and the second-order schemes are considerable while there are some minor differences between the ENO and WENO approximations.

In this test case we found the discrete divergence to be larger than in the other test cases, with L^1 norms in the range 0.1–4.0. Furthermore we did not observe a strong convergence to zero as the mesh was refined. This might be due to the strong shocks present in this test case. However, there is no sign that this affects either the stability or the resolution of the schemes.

3.6 Isothermal blast wave

This test case is taken from [3]. It easily exhibits spurious behavior if the equations are not properly discretized. The equation of state is isothermal in this case, i.e, $p=\rho$, the computational domain is $[0,1]\times[0,1]$ and the initial data are

$$\{\mathbf{u},B_1,B_2,B_3\}_{t=0}=\left\{\mathbf{0},\frac{5}{\sqrt{\pi}},0,0\right\}$$

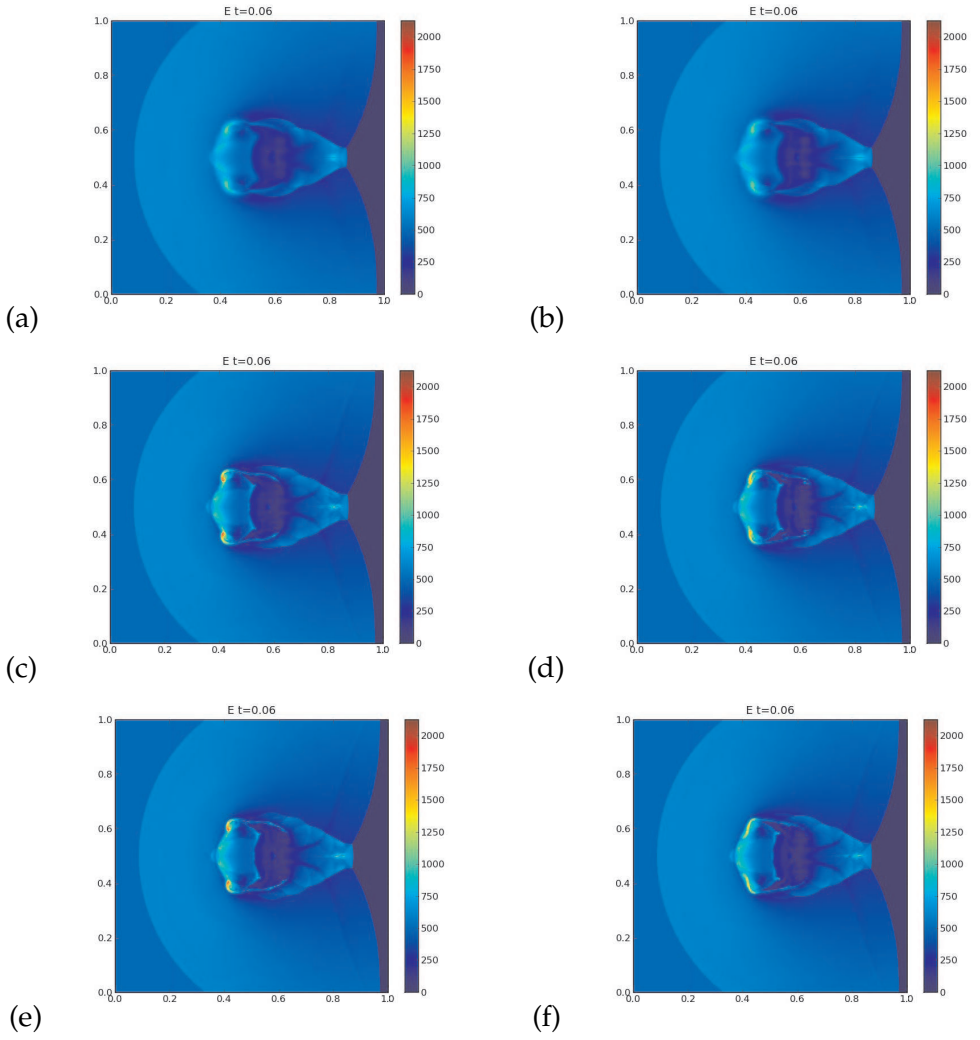

Figure 7: Energy distribution for the cloud-shock interaction on a 1600×1600 mesh at time $t=0.06$. (a) H_3; (b) H_5; (c) H_3E; (d) H_5E; (e) H_3W; (f) H_5W.

and

$$\rho_{t=0}=\begin{cases} 100, & \text{if } |x-0.5|^2+|y-0.5|^2\leq(0.05)^2, \\ 0, & \text{otherwise.} \end{cases}$$

The solution takes the form of a blast wave spreading out from the high density cloud. We test our upwind versions of the Godunov-Powell source term to ascertain whether upwinding the source term imparts numerical stability in this test case. For the sake of clarity, we present the results only with the H_3 and H_3W schemes. Similar results were obtained with the H_5 schemes and with the ENO reconstruction.

In order to illustrate t he necessity of the *upwinded* Godunov-Powell source term, we also considered the central source discretization of (see [36]), and schemes with the Godunov-Powell source set to zero. This lead to the following schemes:

NPH_3	First order three-wave HLL solver with Godunov-Powell source term in (2.3) set to zero,
NPH_3W	second-order WENO version of NPH_3,
CPH_3	first order three-wave HLL solver, central discretization of the Godunov-Po well source term,
CPH_3W	second-order WENO version of CPH_3.

Note that both NPH_3 and CPH_3 use the same numerical flux as H_3 and the only difference is in the source term. Furthermore, the three wave solver obtained by setting the Godunov-Powell source term to zero is different from the standard three wave solver of [21] in this test case as the normal magnetic field is not constant. However, there was very little difference in the numerical results when the three wave solver of [21] was used instead of NPH_3.

We display the computed density (on a logarithmic scale) at time $t = 0.09$ with the above four schemes and H_3, H_3W on a uniform mesh of 400×400 mesh points in Fig. 8. The results presented in Fig. 8 reveal that the first-order version of the three-wave HLL solver works quite well, even when the Godunov-Powell source term is set to zero. This might be on account of the numerical flux, which incorporates some information about the discontinuities in the normal magnetic field. However, the second-order version of the scheme with zero Godunov-Powell source terms led to instabilities as shown in the top right of Fig. 8. The central discretization of the Godunov-Powell source term in (2.3) was unstable even at first-order. The instabilities are manifested as oscillations in the middle left of Fig. 8. The second-order version of this scheme is even more unstable and features large amplitude oscillations as shown in the middle right of Fig. 8. These oscillations continue to grow as the mesh is refined leading to a crash of the central Powell source based scheme on a finer 800×800 mesh. On the other hand, both the H_3 and H_3W schemes show no evidence of the formation of any instabilities (check the bottom row of Fig. 8) at this mesh resolution or at even finer mesh resolutions. Furthermore, the second-order scheme approximates the shock waves quite sharply. These results indicate that not only should the Godunov-Powell source term be introduced, it should also be discretized in a careful upwind manner in-order to obtain numerical stability. The schemes presented in this paper are tailor made for these needs.

3.7 Comparison between the conservative (1.4) and the Godunov-Powell (1.2) forms of the ideal MHD equations

From the discussion in the introduction, the conservative form (1.4) and the semi-conservative Godunov-Powell form (1.2) are equivalent as long as the initial data is di-

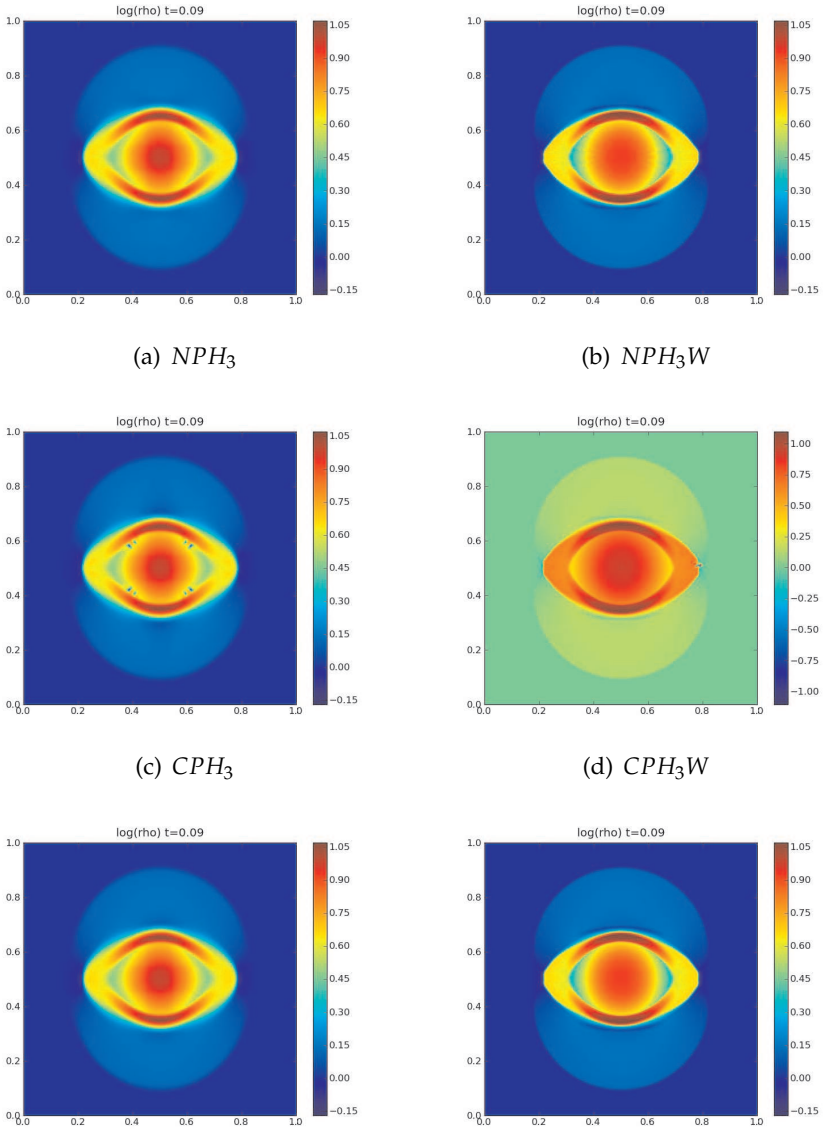

(a) NPH_3 (b) NPH_3W

(c) CPH_3 (d) CPH_3W

(e) H_3 (f) H_3W

Figure 8: Density $(\log(\rho))$ for the Isothermal blast wave at time $t = 0.09$ on a 400^2 mesh. Left Column: First-order. Right Column: Second-order WENO. Top row: Zero Godunov-Powell source. Middle row: Central Godunov-Powell source. Bottom row: Upwind Godunov-Powell source. All figures except middle row, right column use the same scale.

vergence free and the solution remains smooth. However, the non-linearity implies that shock waves and other discontinuities are formed even for smooth initial data and it is not a priori clear if the two forms are equivalent (since we do not have a clear notion of weak solutions to non-conservative equations). In particular, the Godunov-Powell

source term is non-conservative and might lead to different shock speeds and locations when compared to the standard form of the MHD equations. In all the numerical experiments presented above, the shock locations and speeds resulting from the discretization of the Godunov-Powell form are similar to the ones obtained from the conservative form (compare the results presented above with those from [49]), showing that conservation errors are very small. However, one can construct *very special* initial configurations where discretizing the Godunov-Powell form (1.2) results in a different solution than when one discretizes the standard conservative form (1.4) of the ideal MHD equations. We present such a numerical experiment below.

3.7.1 Toth's 2D shock tube

This numerical experiment was constructed in [49] in-order to compare the standard and the Godunov-Powell forms of the MHD equations. It consists of a shock tube with an initial discontinuity that is not aligned with the grid. The initial data are

$$\left(\rho,u_{||},u_{\perp},u_3,B_{||},B_{\perp},B_3,p\right)=\begin{cases}(1,10,0,0,20,5/\sqrt{4\pi},5/\sqrt{4\pi},0), & \text{if } x<y,\\ (1,-10,0,0,20,5/\sqrt{4\pi},5/\sqrt{4\pi},0), & \text{otherwise.}\end{cases}$$

Here we denote the directional components $\{u,B\}_1,\{u,B\}_2$ as $\{u,B\}_{||}$ and $\{u,B\}_{\perp}$ respectively. The computational domain is a narrow strip given by $(x,y)\in[0,1]\times[0,2/N]$ where N is a positive integer. This strip is discretized on a mesh of $N\times 2$ points. Note that the initial magnetic field is constant, hence divergence free. Furthermore, this numerical experiment is essentially one-dimensional as there is no variation in the direction parallel to the initial jump. More details about the set up can be obtained from [49], example 6.3.2. The key observation of [49] in this numerical experiment was that the standard form and the Godunov-Powell form lead to different solutions, particularly for the normal magnetic field $B_{||}$.

We present the results for the normal magnetic field $B_{||}$ in Fig. 9. The results compare the computed normal magnetic field, obtained with the H_3 scheme at two different resolutions ($N=200$ and $N=400$) with the ones obtained with the NPH_3 solver (the three wave solver with the Godunov-Powell source term switched off). A reference one-dimensional solution on a mesh of 1600 points is also shown. The reference solution shows a constant $B_{||}$ as expected, and the three wave HLL solver without the Godunov-Powell source term agrees with this solution except at the discontinuities. On the other hand, the H_3 scheme appears to pick a different solution. On refining the mesh, this difference remains unaltered thus demonstrating that the discretization of the Godunov-Powell source term leads to a distinctly different solution to the one obtained by discretizing the standard form of the MHD equations. The discrepancy from the reference solution is about 2%. This reinforces the observations of [49] regarding the difference of behavior of the two forms of the equations on some shock tube problems where conservation errors can play a role. Using the five-wave solver and the second-order versions of the schemes led to very similar results and we omit them here.

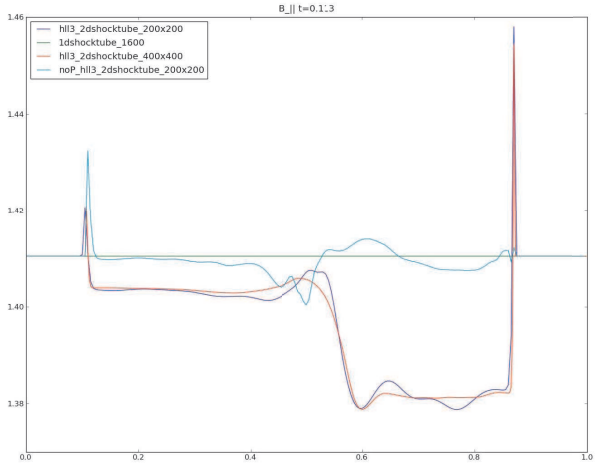

Figure 9: The normal magnetic field $B_{||}$ for the Toth's 2D shock tube with the H_3 scheme (at two different resolutions) and the NPH_3 scheme.

4 Conclusions

We describe highly robust finite volume schemes for the MHD equations based on the semi-conservative *Godunov-Powell* form (1.2). This form is symmetrizable as well as Galilean-invariant, enabling stability estimates (see [6]). Furthermore, the form of the semi-conservative version of the equations in several dimensions is similar to that in one-space dimension, enabling us to design stable one-dimensional schemes that are easily generalized to multidimensional data. The following new numerical elements are found necessary to obtain the desired stability:

• We design HLL-type three-wave and five-wave approximate Riemann solvers that can handle non-constant normal magnetic fields. They can be thought of as extensions of the highly popular three-wave and five-wave solvers of [21] and [34] respectively.

• These HLL-solvers naturally impose an upwind discretization of the Godunov-Powell source term.

• The second-order ENO and WENO-type reconstructions we use are modified to preserve positive pressures and densities.

• We provide a second order extension of the upwind discrete source term.

We test the schemes on a variety of numerical experiments in both one- and two-space dimensions. The results obtained by the schemes (particularly the second-order versions) were impressive, both with respect to stability and accuracy. In particular, the schemes were able to compute the solutions for the advection of varying normal magnetic field in one-dimension and the expected orders of convergence were obtained. A super-fast expansion test illustrated the positivity preservation abilities of the schemes.

The benchmark two-dimensional numerical experiments showed that the schemes

were stable, even on very fine meshes. It is well known that computing two-dimensional MHD on very fine meshes may lead to stability problems and the schemes of this paper were able to handle these fine mesh resolutions. The accuracy of the schemes was very satisfactory on all tests. Among the schemes, the five-wave HLL solver was better in terms of resolution (even at second-order) than the HLL three-wave solver. Similarly the WENO-based schemes were more accurate than the ENO-based schemes. The highly resolved solutions (obtained on very fine meshes) can serve as benchmark reference solutions for future computations. Discrete values of div$\mathbf{B}$ were low in general and reduced as the mesh was refined. Non-zero divergence values did not affect either the stability or the accuracy of the resulting solutions.

Based on the numerical evidence, we conclude that using the semi-conservative form of the MHD equations, with very careful discretizations of the fluxes and the Godunov-Powell source term together with proper high-order reconstructions is a very appealing strategy for designing robust schemes for MHD equations. The numerical tests also indicated that all these ingredients- the introduction of the Godunov-Powell source term, its careful upwind discretization and suitable positivity preserving reconstructions are all necessary for the design of stable schemes. These schemes are easier to comprehend and cheaper computationally than the projection method. Similarly, they are easier to parallelize and to use in conjunction with adaptive mesh refinement than staggering based methods. Numerical experiments illustrating the difference between discretizing the conservative (1.4) and the semi-conservative Godunov-Powell (1.2) are also provided.

These robust schemes are trivial to extend to three dimensions and we aim to employ them for more realistic astrophysical simulations in a forthcoming paper. Also, designing higher than second-order schemes is a work in progress.

References

[1] E. Audusse, F. Bouchut, M. O. Bristeau, R. Klien and B. Perthame, A fast and stable well-balanced scheme with hydrostatic reconstruction for shallow water flows, SIAM. J. Sci. Comp., 25(6) (2004), 2050–2065.

[2] D. S. Balsara and D. Spicer, A staggered mesh algorithm using high order Godunov fluxes to ensure solenoidal magnetic fields in magnetohydrodynamic simulations, J. Comp. Phys., 149(2) (1999), 270–292.

[3] D. S. Balsara, Total variation diminishing algorithm for adiabatic and isothermal magnetohydrodynamics, Astrophys. J. Supp. Ser., 116 (1998), 133–153.

[4] D. S. Balsara, Divergence-free reconstructions of magnetic fields and WENO schemes for magnetohydrodynamics, J. Comp. Phys., 228(14) (2009), 5040–5056.

[5] D. S. Balsara, T. Rumpf, M. Dumbser and C. D. Munz, Efficient high accuracy ADER-WENO schemes for hydrodynamics and divergence-free MHD, J. Comp. Phys., 228(7) (2009), 2480–2516.

[6] T. J. Barth, Numerical methods for gas dynamics systems, in: An introduction to Recent Developments in Theory and Numerics for Conservation Laws, D. Kröner, M. Ohlberger, C. Rohde (Eds.), Springer, 1999.

[7] C. Berthon, Why the MUSCL-Hancock scheme is L^1-stable, Numer. Math., 104 (2006), 27–46.

[8] F. Bouchut, C. Klingenberg and K. Waagan, A multi-wave HLL approximate Riemann solver for ideal MHD based on relaxation I- theoretical framework, Numer. Math., 108(1) (2007), 7–42.
[9] F. Bouchut, C. Klingenberg and K. Waagan, A multi-wave HLL approximate Riemann solver for ideal MHD based on relaxation II-numerical experiments, Preprint, 2008.
[10] J. U. Brackbill and D. C. Barnes, The effect of nonzero div$B$ on the numerical solution of the magnetohydrodynamic equations, J. Comp. Phys., 35 (1980), 426–430.
[11] M. Brio and C. C. Wu, An upwind differencing scheme for the equations of ideal MHD, J. Comp. Phys., 75(2) (1988), 400–422.
[12] P. Cargo and G. Gallice, Roe matrices for ideal MHD and systematic construction of Roe matrices for systems of conservation laws, J. Comp. Phys., 136(2) (1997), 446–466.
[13] W. Dai and P. R. Woodward, A simple finite difference scheme for multi-dimensional magnetohydrodynamic equations, J. Comp. Phys., 142(2) (1998), 331–369.
[14] A. Dedner, F. Kemm, D. Kröner, C. D. Munz, T. Schnitzer and M. Wesenberg, Hyperbolic divergence cleaning for the MHD equations, J. Comp. Phys., 175 (2002), 645–673.
[15] B. Einfeldt, On the Godunov type methods for gas dynamics, SIAM. J. Num. Anal., 25(2) (1988), 294–318.
[16] C. Evans and J. F. Hawley, Simulation of magnetohydrodynamic flow: a constrained transport method, Astrophys. J., 332 (1998), 659–677.
[17] F. Fuchs, K. H. Karlsen, S. Mishra and N. H. Risebro, Stable upwind schemes for the magnetic induction equation, Math. Model. Num. Anal., 43(5) (2009), 825–852.
[18] F. Fuchs, S. Mishra and N. H. Risebro, Splitting based finite volume schemes for the ideal MHD equations, J. Comp. Phys., 228(3) (2009), 641–660.
[19] F. Fuchs, A. D. McMurry, S. Mishra and N. H. Risebro, Finite volume methods for wave propagation in stratified magneto-atmospheres, Commun. Comput. Phys., to appear, 2010.
[20] S. K. Godunov, The symmetric form of magnetohydrodynamics equation, Num. Meth. Mech. Cont. Med., 1 (1972), 26–34.
[21] K. F. Gurski, An HLLC-type approximate Riemann solver for ideal Magneto-hydro dynamics, SIAM. J. Sci. Comp., 25(6) (2004), 2165–2187.
[22] S. Gottlieb, C. W. Shu and E. Tadmor, High order time discretizations with strong stability property, SIAM. Rev., 43 (2001), 89–112.
[23] A. Harten, B. Engquist, S. Osher and S. R. Chakravarty, Uniformly high order accurate essentially non-oscillatory schemes, J. Comp. Phys., 71 (1987), 231–303.
[24] A. Harten, P. D. Lax and B. Van Leer, On upstream differencing and Godunov type schemes for hyperbolic conservation laws, SIAM. Rev., 25(1) (1983), 35–61.
[25] V. Honkkila and P. Janhunen, HLLC solver for ideal relativistic MHD, J. Comp. Phys., 223 (2007), 643–656.
[26] V. L. Kolgan, Application of the minimum-derivative principle in the construction of finite-difference schemes for the numerical analysis of discontinuous solutions in gas dynamics, Transactions of the Central Aerohydrodynamics Institute, 3(6) (1972), 68–77.
[27] V. L. Kolgan, Finite-difference schemes for computation of three dimensional solutions of gas dynamics and calculation of a flow over a body under an angle of attack, Transactions of the Central Aerohydrodynamics Institute, 6(2) (1975), 1–6.
[28] R. J. LeVeque, Finite Volume Methods for Hyperbolic Problems, Cambridge University Press, Cambridge, 2002.
[29] R. J. LeVeque, Wave propagation algorithms for multi-dimensional hyperbolic systems, J. Comp. Phys., 131 (1997), 327–353.

[30] S. Li, An HLLC Riemann solver for magneto-hydrodynamics, J. Comp. Phys., 203 (2005), 344–357.
[31] T. J. Linde, A Three Adaptive Multi Fluid MHD Model for the Heliosphere, Ph.D thesis, University of Michigan, Ann-Arbor, 1998.
[32] P. Londrillo and L. del Zanna, On the divergence-free condition in Godunov-type schemes for ideal magnetohydrodynamics: the upwind constrained transport method, J. Comp. Phys., 195(1) (2004), 17–48.
[33] S. Mishra and E. Tadmor, Constraint preserving schemes using potential-based fluxes: III, genuinely multi-dimensional central schemes for MHD equations, Preprint, 2009.
[34] T. Miyoshi and K. Kusano, A multi-state HLL approximate Riemann solver for ideal magneto hydro dynamics, J. Comp. Phys., 208(1) (2005), 315–344.
[35] K. G. Powell, An approximate Riemann solver for magneto-hydro dynamics (that works in more than one space dimension), Technical Report, 94–24, ICASE, Langley, VA, 1994.
[36] K. G. Powell, P. L. Roe, T. J. Linde, T. I. Gombosi and D. L. De zeeuw, A solution adaptive upwind scheme for ideal MHD, J. Comp. Phys., 154(2) (1999), 284–309.
[37] P. L. Roe and D. S. Balsara, Notes on the eigensystem of magnetohydrodynamics, SIAM. J. Appl. Math., 56(1) (1996), 57–67.
[38] J. Rossmanith, A Wave Propagation Method with Constrained Transport for Shallow Water and Ideal Magnetohydrodynamics, Ph.D thesis, University of Washington, Seattle, 2002.
[39] D. S. Ryu, F. Miniati, T. W. Jones and A. Frank, A divergence free upwind code for multidimensional magnetohydrodynamic flows, Astrophys. J., 509(1) (1988), 244–255.
[40] C. W. Shu and S. Osher, Efficient implementation of essentially non-oscillatory schemes-II, J. Comp. Phys., 83 (1989), 32–78.
[41] J. M. Stone, T.A. Gardiner, A. Thomas, P. Teuben, J. F. Hawley and J. B. Simon, Athena: a new code for astrophysical MHD, Astrophys. J. Supp. Ser., 178(1) (2008), 137–177.
[42] E. F. Toro, Riemann Solvers and Numerical Methods for Fluid Dynamics, Springer Verlag, third edition, 2009.
[43] E. F. Toro, M. Spruce and W. Speares, Restoration of the contact surface in the HLL Riemann solver, Tech. Report COA-9204, College of Aeronautics, Cranfield Institute of Technology, U.K., 1992.
[44] E. F. Toro, M. Spruce and W. Speares, Restoration of the contact surface in the Harten-Lax-van Leer Riemann solver, Shock. Waves., 4 (1994), 25–34.
[45] M. Torrilhon and M. Fey, Constraint-preserving upwind methods for multidimensional advection equations, SIAM. J. Num. Anal., 42(4) (2004), 1694–1728.
[46] M. Torrilhon, Locally divergence preserving upwind finite volume schemes for magnetohyrodynamic equations, SIAM. J. Sci. Comp., 26(4) (2005), 1166–1191.
[47] M. Torrilhon, Uniqueness conditions for Riemann problems of ideal Magnetohydrodynamics, J. Plasma. Phys., 69(3) (2003), 253–276.
[48] M. Torrilhon and D. S. Balsara, High-order WENO schemes: investigations on non-uniform convergence for MHD Riemann problems, J. Comp. Phys., 201(2) (2004), 586–600.
[49] G. Toth. The div$B=0$ constraint in shock capturing magnetohydrodynamics codes, J. Comp. Phys., 161 (2000), 605–652.
[50] B. Van Leer, Towards the ultimate conservative difference scheme. V, J. Comp. Phys., 32 (1979), 101–136.
[51] K. Waagan, A positive MUSCL-Hancock scheme for ideal MHD, J. Comp. Phys., to appear.